Sustainable Energy & Fuels

ROYAL SOCIETY OF CHEMISTRY

PAPER

View Article Online
View Journal | View Issue

Cite this: *Sustainable Energy Fuels*, 2024, **8**, 4243

Techno-economic analysis of a solar-driven biomass pyrolysis plant for bio-oil and biochar production†

Muhammad Ahsan Amjed, *[ab] Filip Sobic, [a] Matteo C. Romano, [a] Tiziano Faravelli [b] and Marco Binotti *[a]

Pyrolysis has become one of the most attractive options for converting carbonaceous biomass into bio-oil or biochar. This study explores a novel solar pyrolysis process intended to produce both bio-oil and biochar, thereby improving carbon efficiency. Aspen Plus and SolarPILOT were used to model a 10 MW biomass pyrolysis plant thermally sustained by hot particles from a falling-particle solar tower receiver. A yearly analysis was carried out for three configurations to estimate the annual production of oil and biochar. The results showed that the hybrid plant, combining solar receiver and biochar backup combustor, leads to the lowest cost of bio-oil (18.7 € per GJ, or 0.29 € per kg) and a carbon efficiency of 83%. Whereas, the plant fully sustained by solar power achieves a carbon efficiency of 90%; however, it results in a significantly higher cost of bio-oil (21.8 € per GJ, or 0.34 € per kg) due to the larger size of particle storage and a lower capacity factor of the pyrolysis plant. In comparison, a conventional pyrolysis plant with no biochar production yielded the most expensive option in terms of the cost of produced bio-oil (27.5 € per GJ) and features the lowest carbon efficiency (74%). Sensitivity analysis shows that the pyrolyzer Capex, operational cost, biochar market price, plant availability and discount rate significantly affect bio-oil production cost.

Received 3rd April 2024
Accepted 22nd July 2024

DOI: 10.1039/d4se00450g

rsc.li/sustainable-energy

1. Introduction

Bioenergy provides 12.6% of the overall energy consumption and is one of the most significant renewable energy sources in the world's energy mix.[1] There are two main pathways for converting biomass into higher-density energy vectors, namely biochemical and thermochemical pathways. Thermochemical conversion benefits from faster chemical reactions, and it is suitable for a wider variety of biomass feedstock compared to the biochemical process. Moreover, thermochemical conversion is not subjected to seasonal and environmental limitations as a biochemical process and allows year-round operations with a better control of operating conditions. In addition, it has high energy efficiency and advantages of scalability over biochemical process.[2] Based on the amount of supplied oxygen, thermochemical processes can be classified as pyrolysis, combustion or gasification.[3] Among them, pyrolysis has received great attention due to its capability of converting virtually any type of solid biomass into bio-oil and/or biochar, which is a high-potential option for improving soil quality and carbon dioxide removal (CDR).[4,5]

The pyrolysis process is endothermic and requires an external source of energy to heat up the feedstock and break down the molecular structure of the carbonaceous material. This thermal input can be supplied by various sources, *e.g.* direct combustion of its by-products, electrical resistive heating or solar thermal heating.[6,7] The limit of conventional pyrolysis processes sustained by combustion is the loss of part of the biogenic carbon as CO_2. Supplying the process heat *via* electric or solar heating allows for the reduction of CO_2 emissions and improves the carbon efficiency and the amount of bio-based products.

Concentrated solar power (CSP) systems use a series of mirrors that concentrate the solar radiation towards a receiver where solar energy is converted into thermal energy, which can either be used directly or to produce electricity using a thermodynamic cycle. The possibility of storing heat in a low-cost thermal energy storage (TES) system for later use allows for decoupling the availability of solar radiation from thermal power production. In contrast to solar photovoltaics (PV), CSP systems use almost the entire spectrum of solar radiation to produce heat typically in the range of 400–2000 °C, which may be used to drive chemical reactions such as pyrolysis.[8,9] The integration of CSP into conventional pyrolysis may help fulfil

[a]*Department of Energy, Politecnico di Milano, via Lambruschini 4, 20156, Milano, Italy. E-mail: muhammadahsan.amjed@polimi.it; marco.binotti@polimi.it*

[b]*Department of Chemistry, Materials, and Chemical Engineering, "G. Natta", CRECK Modelling Lab, Politecnico di Milano, Piazza Leonardo da Vinci 32, 20133, Milano, Italy*

† Electronic supplementary information (ESI) available. See DOI: https://doi.org/10.1039/d4se00450g

the energy requirements of the endothermic pyrolysis reactor.[6,10,11]

Joardder *et al.*[12] conducted a lab scale study, in which solar radiation was directly focused on a pyrolysis reactor. The results show that solar-based pyrolysis can cut 33% of fuel production costs and 32.4% of carbon emissions. Moreover, combining CSP with conventional pyrolysis allows for the storage of solar thermal energy in terms of transportable, high energy density and upgraded fuel.[10,13] It also reduces reactor dependency on its by-product combustion, which ultimately reduces its carbon footprint.[14,15]

Other studies have investigated the integration of CSP in the conventional pyrolysis of biomass using direct radiation on a reactor in a lab-scale environment in which multiple types of biomasses went through a thermochemical conversion process with CSP assistance.[6,16–21] In addition to biomass, the solar pyrolysis of other feedstocks was assessed. For instance, Zeaiter *et al.*[22] assessed the pyrolysis of scrap rubber using Fresnel lenses to concentrate the radiation over a tube filled with feedstock, with and without a catalyst. Hosseini *et al.*[8] recently modeled coal drying and pyrolysis using CSP under four different scenarios considering different collectors, pyrolysis temperatures, and heat transfer fluids (HTF). They found that the integration of solar towers at optimized sizes of solar multiple and storage can meet 12.8% of the annual thermal energy demand for the drying and pyrolysis of coal.

In some lab scale studies,[6,12,16,19–23] fixed bed or rotating pyrolysis reactors were used with solar radiation directly concentrated onto the reactor surface by Fresnel lenses or parabolic dishes, which attained low and medium temperature ranges from 250 to 600 °C based on design parameters and pyrolysis reactor requirements.

Many types of CSP systems can be used for solar pyrolysis, *e.g.* dishes, linear concentrators and power towers.[10,24] Contrarily to conventional power towers, which typically adopt molten salts as a heat transfer medium, this work considers advanced falling particle tower systems, recently proposed as advanced solutions for next-generation CSP systems.[25] The main idea behind the falling particle receiver is to avoid the maximum temperature limit given by the stability of the molten salts (~565 °C), allowing for direct heating of the particles, which enables increasing the peak flux on the receiver from 1 MW m^{-2} in the case of conventional receivers to at least 2 MW m^{-2}.[26] In the case of pyrolysis, another important advantage is the possibility of using these particles directly in the reactor, thus avoiding the use of an intermediate heat exchanger. A recent comparative study by Jie Ling *et al.*[27] also suggested the above-mentioned claim and proposed a CSP beam-down tower and solid particle receiver with a fluidized reactor for high efficiency and high-temperature solar pyrolysis operations.

Previous studies on CSP-based pyrolysis predominantly focus on small-scale laboratory experiments involving direct irradiation on the reactor. The solar-driven pyrolysis using direct radiation faces several challenges, including uneven heat distribution within the reactor, thermal stress caused by variations in solar flux, and lower oil yields due to the slow pyrolysis of biomass. Furthermore, there is no control over the temperature and heating rates, and the process stops working in the absence of sunlight.[7,10] To address these issues while maintaining the concept of fast pyrolysis using a fluidized bed reactor, indirect solar CSP heating was adopted through solid PHCs. This solution also offers thermal storage for longer periods in the absence of sunlight, ensuring the smooth operation of pyrolysis.

There is a notable absence of studies examining CSP-based pyrolysis with solid PHC falling particle receivers on an industrial scale. Moreover, there is a significant gap in the literature regarding the techno-economic analysis of such industrial-scale solar-assisted pyrolysis plants. Our work aims to address this gap and serves as a starting point for future projects in this area. To the best of our knowledge, this work explores for the first time the process integration of an industrial scale biomass pyrolysis plant with a falling particle solar tower system using the same solid particle heat carrier (PHC) for the biomass pyrolysis reactor and as a heat carrier in the solar receiver. The main purpose of this study, which is conducted as part of the EU Pysolo project,[28] is to perform a techno-economic assessment of 10 MW_{th} fast pyrolysis plants for bio-oil and biochar production integrated with a falling particle solar tower system, starting from existing industrial scale models for the pyrolysis process and CSP system. The following three cases are assessed and compared through techno-economic indicators:

- Conventional pyrolysis process: reference configuration, where the heat for the pyrolysis process is supplied through the combustion of a fraction of the pyrolysis products (char and pyro-gases).
- Solar-based pyrolysis process: heat for the pyrolysis process is provided only by solar heat produced using the CSP system equipped with a Thermal Energy Storage (TES) system, and all the produced biochars is exported as products.
- Hybrid pyrolysis process: heat for the pyrolysis process is supplied either from the CSP system or, when no solar heat is available, from the combustion of a fraction of the pyrolysis products, resulting in the export of most of the biochar produced.

2. Methods

The configuration of the fast pyrolysis section for the base case is taken from Jones *et al.*,[29] where a biorefinery converting woody biomass into high-value liquid fuel was modelled. To compute the mass and energy balances of the pyrolysis plant, the process simulation software Aspen Plus 10 is used.[30] As the detailed description of the complex chemical reactions occurring in the fast pyrolysis reactor is out of the scope of the current study, the pyrolyzer is modeled as a black box with fixed biomass input, replicating the yield and product composition reported by Jones *et al.*[29] In all three assumed cases, the impact of thermodynamics and operating conditions on product yield and quality is not considered. Instead, the product yield and operating parameters were kept constant to maintain consistency in the techno-economic analysis.

Woody biomass of poplar tree that grows abundantly in Europe, Canada and South America is considered biomass

feedstock. The plant is sized to convert a biomass input of 50 dry t per h (10 MW_{th} on a lower heating value basis). The relatively small plant size is representative of a scenario of multiple pyrolysis plants erected at a biomass point source aimed at generating a high volumetric energy density product to be transported to a central refining plant. Transportation of compact products instead of bulky biomass from point sources helps reduce both transportation costs and carbon emissions. The main assumptions for modeling the pyrolysis plant are as follows:

(1) The plant operates under steady-state conditions.

(2) All the plant equipment is modelled with a zero-dimensional approach.

(3) Particle Heat Carriers (PHC) used in the model are considered chemically inert in the pyrolysis reactor.

A block diagram of the conventional pyrolysis section is depicted in Fig. 1A. Biomass is initially dried using hot flue gases obtained from the combustion of pyrolysis products. Then, it is fed to a fast pyrolysis fluidized bed reactor (FBR) together with hot PHC and used as a heat carrier. The solid products and the PHC exiting the pyrolysis reactor are then sent to a combustor, where the combustion of char increases the PHC temperature before it is recirculated to the FBR. The gaseous products exiting the FBR are then cooled and separated in non-condensable pyro-gases, partly recirculated to the reactor and partly combusted to thermally sustain the process.

A schematic of the solar-driven pyrolysis plant is reported in Fig. 1B. In this configuration, the solid PHC and char exiting the FBR are separated. The PHC particles are sent back to the CSP section of the plant, and the biochar is extracted from the plant as an additional product. The CSP section includes the falling particle receiver on top of the power tower and the TES system.

Table 1 Properties of adopted biomass (poplar)

Elemental analysis (% wt on dry basis)	
C	50.94
H	6.04
O	41.90
N	0.17
S	0.03
Ashes	0.92
Proximate analysis (% wt on dry basis)	
Volatile matters	84.88
Fixed carbon	14.2
Ashes	0.92
Sulfur analysis (% wt on dry basis)	
Pyritic sulfur	0.03
Sulphate	0.00
Organic sulfur	0.00
Calorific values (MJ kg^{-1})	
HHV	14.0
LHV	12.3
Humidity, dry basis	30%

In the receiver, the solid particles acting as PHC are directly irradiated to raise their temperature and then sent back to the FBR. The solar field is modelled using SolarPILOT,[31] a software developed by NREL for the design and performance simulation of power tower heliostat fields, while the falling particle receiver is modelled with an in-house code.[32]

For the solar-based pyrolysis plant, two PHCs are considered (sand and ceramic particles), and two different operational modes are considered (solar only and hybrid mode). For each plant, a yearly product yield is assessed, together with annual

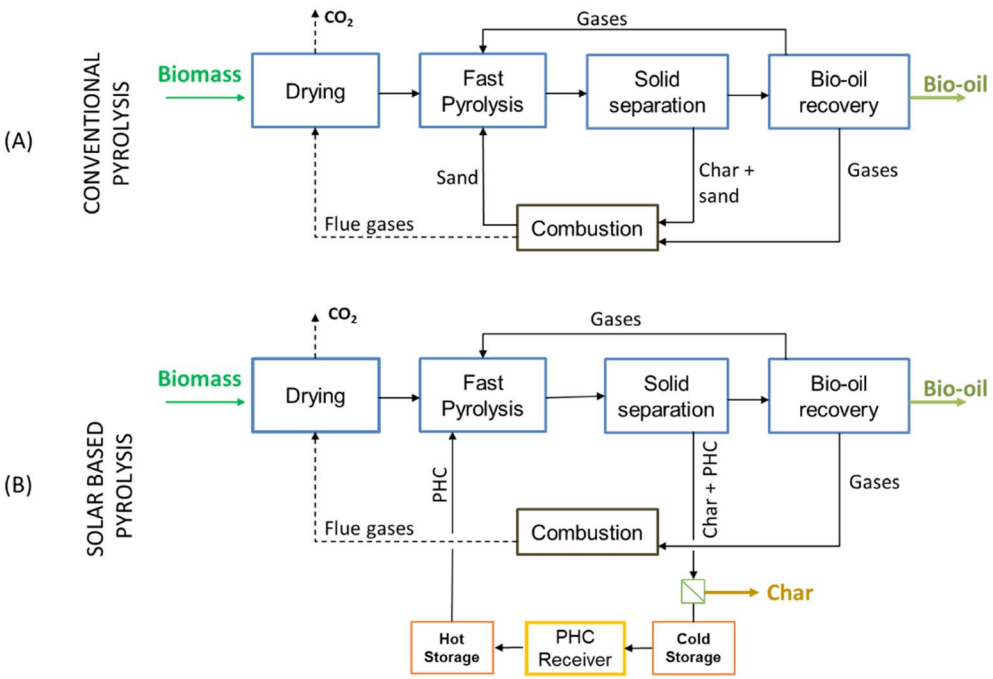

Fig. 1 Block diagram of the conventional (A) and solar-based (B) pyrolysis plants.

emission, CSP plant efficiencies, energy conversion efficiencies, minimum fuel sale price (MFSP) and availability.

The biomass considered in the model is hybrid poplar wood, with thermochemical analysis data presented in Table 1. For ambient air, summer conditions are assumed (32.2 °C, 10 132 bar, 75.5% relative humidity).[29] The thermochemical properties of all the species used in Aspen Plus to model pyrolysis products are given in ESI Section 1.†

2.1. Key performance indicators

This section presents the key performance indicators (KPIs) used to compare different plants.

Pyrolysis plant energy conversion efficiency $\eta_{\text{pyro plant}}$ is calculated by applying eqn (1):

$$\eta_{\text{pyro plant}} = \frac{\sum_i \dot{m}_{\text{prod},i} \times \text{LHV}_{\text{prod},i}}{\dot{m}_{\text{biom}} \times \text{LHV}_{\text{biom}} + \left(\frac{P_{\text{Aux}}}{\eta_{\text{el,ref}}}\right) + \dot{Q}_{\text{PHC}}}, \quad (1)$$

where $\dot{m}_{\text{prod},i}$ and $\text{LHV}_{\text{prod},i}$ are the mass flow rate and Lower Heating Value (LHV) of i^{th} product, respectively. The pyrolysis products are biochar, sludge, bio-oil and some gaseous products. The denominator represents the primary energy input, where $\dot{m}_{\text{biom}}$ and LHV_{biom} are the mass flow rate and LHV of biomass, respectively, P_{Aux} is the power of auxiliaries for compressors and heat rejection units, $\eta_{\text{el,ref}}$ is the reference thermal to electrical energy efficiency (assumed equal to 50% [25]) and $\dot{Q}_{\text{PHC}}$ is the thermal power provided *via* the PHC to the pyrolysis unit.

The CSP plant solar-to-thermal efficiency $\eta_{\text{sol-th}}$ is calculated by applying eqn (2) as the product of the solar field optical efficiency, η_{opt}, and of the falling particle receiver thermal efficiency, $\eta_{\text{th,rec}}$. $\dot{Q}_{\text{rec}}$ and $\dot{Q}_{\text{PHC,rec}}$ are the solar power incident on the receiver and thermal power delivered to PHC, respectively. DNI is the direct normal irradiance and A_{h} is the total heliostat area.

$$\eta_{\text{sol-th}} = \eta_{\text{opt}} \times \eta_{\text{th,rec}} = \frac{\dot{Q}_{\text{rec}}}{A_{\text{h}} \times \text{DNI}} \times \frac{\dot{Q}_{\text{PHC,rec}}}{\dot{Q}_{\text{rec}}} = \frac{\dot{Q}_{\text{PHC,rec}}}{A_{\text{h}} \times \text{DNI}}. \quad (2)$$

Carbon efficiency ε_{C} is calculated using eqn (3), where $y_{\text{C,prod},i}$ and $y_{\text{C,biom}}$ are the carbon content in i^{th} product and biomass, respectively.

$$\varepsilon_{\text{C}} = \frac{\sum_i \dot{m}_{\text{prod},i} \times y_{\text{C,prod},i}}{\dot{m}_{\text{biom}} \times y_{\text{C,biom}}}. \quad (3)$$

The thermal energy usage efficiency of the CSP-based pyrolysis plant $\eta_{\text{th,use}}$ is calculated using eqn (4), where $\dot{Q}_{\text{def}}$ is the total solar power loss through defocusing.

$$\eta_{\text{th,use}} = 1 - \frac{\dot{Q}_{\text{def}}}{\dot{Q}_{\text{PHC,rec}}}. \quad (4)$$

Emission to oil ratio (ETO) is calculated using eqn (5). E and Oil are the CO_2 emissions and oil production in kg and GJ, respectively, from the pyrolysis plant.

$$\text{ETO} = \frac{E}{\text{Oil}}. \quad (5)$$

Considering that biogenic CO_2 emissions are climate neutral, CO_2 emission credits associated with biochar production are also computed as net negative emission to oil ratio (ETO_{net}) using eqn (6).

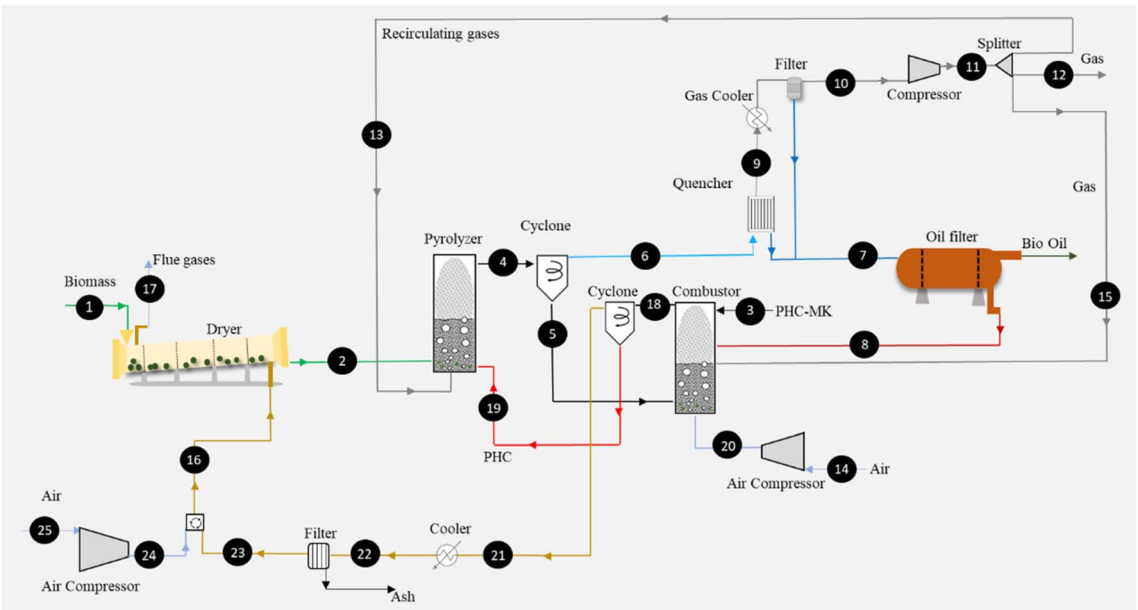

Fig. 2 Schematic diagram of the modelled conventional pyrolysis plant.

$$\mathrm{ETO}_{\mathrm{net}} = -\frac{\dot{m}_{\mathrm{char},i} \times y_{\mathrm{C,char}} \times \frac{44}{12}}{\mathrm{Oil}_t}. \quad (6)$$

3. Conventional pyrolysis plant

3.1. Plant configuration and component modeling

The biomass pyrolysis plant, whose schematic is depicted in Fig. 2, is divided into the following five sections:

- Section 1, Biomass pretreatment: The first section comprises the preparation of biomass before the pyrolysis process *via* drying and grinding.
- Section 2, Pyrolysis: This section consists of a fluidized bed pyrolysis reactor, where dried biomass is converted by contact with hot PHC and fluidizing gases.
- Section 3, Solid removal: It encompasses the cyclone filter, which is responsible for the separation of volatile products from solids entrained from the reactor at high temperatures.
- Section 4, Bio-oil recovery: In this section, quenching columns are used for the condensation and collection of bio-oil along with other auxiliaries and bio-oil filters.
- Section 5, Combustion: This section includes the combustor block, where biochar, a portion of pyrolytic gases, and retentate of the filter are burnt to heat the circulating PHC.

Section 1: Biomass pretreatment. Biomass feedstock is fed to the plant at 20 °C. For efficient conversion, the biomass undergoes a drying process before being fed to the pyrolizer. The biomass size is reduced to 2 mm by a grinder, which is connected to a direct rotary dryer. This process speeds up the pyrolysis within the fluidized bed reactor (Fig. 2).

A single-pass direct feed dryer is assumed to consist of a rotating drum where biomass is put in contact with the hot gases, which provide the required heat for drying. The biomass is collected from the outlet as the drum rotates, while the humid gases are vented into the atmosphere. For this type of dryer, the inlet hot gases have a temperature between 230 °C and 1100 °C and an outlet temperature between 70 °C and 110 °C to prevent condensation of moisture in the vapor stream.[33]

The biomass temperature and residual moisture at the dryer exit (stream 2) were assumed to be equal to 71.7 °C and 10%, respectively. The temperature of the hot gases (stream 16) fed to the dryer is reduced by mixing ambient air (stream 25) with flue gases exiting the combustor (steam 23). ESI Table 3† reports the parameters assumed in the simulation.

Sections 2 and 3: Pyrolysis and solid removal. After drying and pretreatment, biomass is fed to the fluidized bed pyrolysis reactor (FBR) together with hot PHC exiting the combustor. A portion of the incondensable gases is recirculated into the FBR after quenching. The temperature of the PHC fed to the FBR is equal to 609 °C, and its flow rate is controlled to maintain a reactor exit temperature of 434 °C.

An RYield reactor with a fixed outlet composition, operating temperature and pressure obtained from the study by Jones *et al.*[29] is adopted in Aspen Plus to model the reactor. Table 2 describes the product yield from the pyrolysis reactor.

Downstream of the pyrolyzer, all products flow into the solid separation unit, which consists of a cyclone filter to remove almost all solids from hot vapors. Solid materials, mainly PHC, char and ashes, are transferred to the combustor, while volatile matter is directed to the condensation unit. The PHC separation efficiency is assumed to be 99.9% while the char and ash separation efficiency is assumed to be 92% because of the finer particle sizes. ESI Table 4† depicts the assumptions and parameters used in this plant section.

Section 4: Bio-oil recovery. In this section, the pyrolysis vapors are cooled in two condensers to recover the liquid product. The first condenser (quencher) uses air to cool the pyrolysis vapors to 70 °C, condenses the heavier species and turns them into liquid oil. The second condenser uses cooling water to increase bio-oil recovery by cooling the pyrolysis vapors to 45 °C. Substances remaining in the gaseous phase are incondensable species that finally pass through the demister to separate aerosols, mainly comprising organic residue and water droplets suspended in the gaseous stream. These entrained aerosols are removed to avoid problems in the downstream compression unit. The compressed gases are then separated and mostly (96%) recirculated to the FBR as fluidization gas. The remaining portion is split between the combustor (about 2% of the total flow) and an output pyro-gas byproduct stream (the remaining is ~2%). The outlet pyro-gas can be used as a feedstock in the possible downstream upgrade process of bio-oil or as fuel for power generation. The process parameters used in the bio-oil recovery model are illustrated in ESI Table 5.†

Before storage, bio-oil passes through the filtration process, where solid particles are removed along with a small portion of oil (stream 8). This is burnt together with other components in the combustor to fulfil the energy needs of the reactor.

Section 5: Combustion. The inputs to the combustor are solids (stream 5), which are collected from the pyrolytic vapors, the retentate produced by the bio-oil filter (stream 8) and the

Table 2 Composition of pyrolysis products (stream 4, Fig. 2) considered in the model

Species	Concentration (% wt)	Species	Concentration (% wt)	Species	Concentration (% wt)	Species	Concentration (% wt)
H_2O	5.89	C_2H_6	0.64	$C_3H_6O_2$	1.30	$C_{12}H_8O$	0.35
H_2	0.07	C_3H_8	0.02	$C_6H_6O_2$	1.09	$C_{20}H_{26}O_8$	1.43
O_2	0.19	C_4H_{10}	0.00	$C_{10}H_{12}O_2$	0.78	$C_{21}H_{26}O_8$	0.31
N_2	0.04	C_2H_4	1.46	$C_6H_{10}O_5$	0.93	$C_8H_{11}N$	0.01
CO	34.88	C_3H_6	1.02	$C_{12}H_{22}O_{11}$	5.29	S	0.01
CO_2	32.87	$C_4H_6O_2$	0.87	$C_{20}H_{28}O_2$	0.47	C	2.42
CH_4	4.63	$C_8H_8O_3$	1.09	$C_{16}H_{16}O_2$	1.71	ASH	0.22

incondensable gases (stream 15). The PHC recovered from the pyrolyzer (stream 5) is transferred to the combustor for reheating, along with a PHC make-up flow (PHC-MK) added to compensate for PHC losses. The combustor increases the temperature of the PHC to 609 °C.[29]

Combustion is carried out with ambient air, with 25% excess with respect to stoichiometric combustion. Thermal losses in the combustor are assumed to be equal to 1% of the biomass LHV. Downstream of the combustor, the hot PHC is separated by applying a cyclone and recirculating it to the pyrolyzer. The resulting hot gas is cooled and diluted with air to achieve 345.5 °C at the dryer inlet. Entrained ashes along with a small quantity of PHC are separated by filtration air dilution, and the drying gas temperature is tuned to achieve a target dryer exit temperature of 71.7 °C.[29] ESI Table 6† lists the assumptions and parameters used to model the combustion section.

4. Solar-based pyrolysis

4.1. Plant configuration

To overcome the intensive energy needs of pyrolysis and to reduce its carbon footprint, a Concentrated Solar Power (CSP) plant is introduced in the system. CSP replaces the combustor block in the process model of conventional pyrolysis and provides the required thermal energy to the pyrolysis reactor. Recovering biochar reduces the emissions of carbon dioxide (as well as of NO_x and particulate matter) related to the combustion of biochar and other organic byproducts. The following changes are introduced in the CSP-based pyrolysis plant with respect to the conventional pyrolysis case:

(1) Introduction of CSP block to replace the biochar combustor;

(2) Introduction of an additional combustor for the combustion of excess gases for biomass drying;

(3) Introduction of biochar cooling and recovery unit.

Fig. 3 shows a schematic of the integrated process considering the above-mentioned changes. The pyrolizer outlet stream (stream 4) passes through a cyclone, where solid particles are separated from pyrolysis vapors. Solids are then sent to a char-PHC separator, where char is recovered and PHC is returned to the CSP loop. Char/PHC separation is expected to be a challenging process that may be obtained using different solid/solid separation techniques by exploiting the different particle sizes and densities. In the presented analysis, char separation efficiency from PHC is assumed to be equal to 99.99%. A PHC make up (PHC-MK) is considered to account for losses during the separation of char and PHC. The separated PHC and make-up PHC flows are heated up to the same target temperature as the baseline plant (609 °C) in the CSP unit. ESI Table 7† illustrates the parameters used in CSP-based pyrolysis after changes in the conventional pyrolysis model.

In the CSP-based process, one combustor block is included to generate hot gases for the dryer. In this case, as char is recovered as an additional product, only light gaseous products are burnt in the combustor. The hot gases exiting the combustor are partly cooled before feeding the dryer *via* heat exchange and air mixing to avoid the loss of biomass volatiles in the drying process.

4.2. CSP plant modelling

Concentrated Solar Power (CSP) section consists of three main subsystems: solar field, falling particle receiver, and Thermal Energy Storage (TES) system. Cold particles are elevated using a particle elevator at the top of the solar tower. Then, these particles fall from the top of the receiver, where they are directly

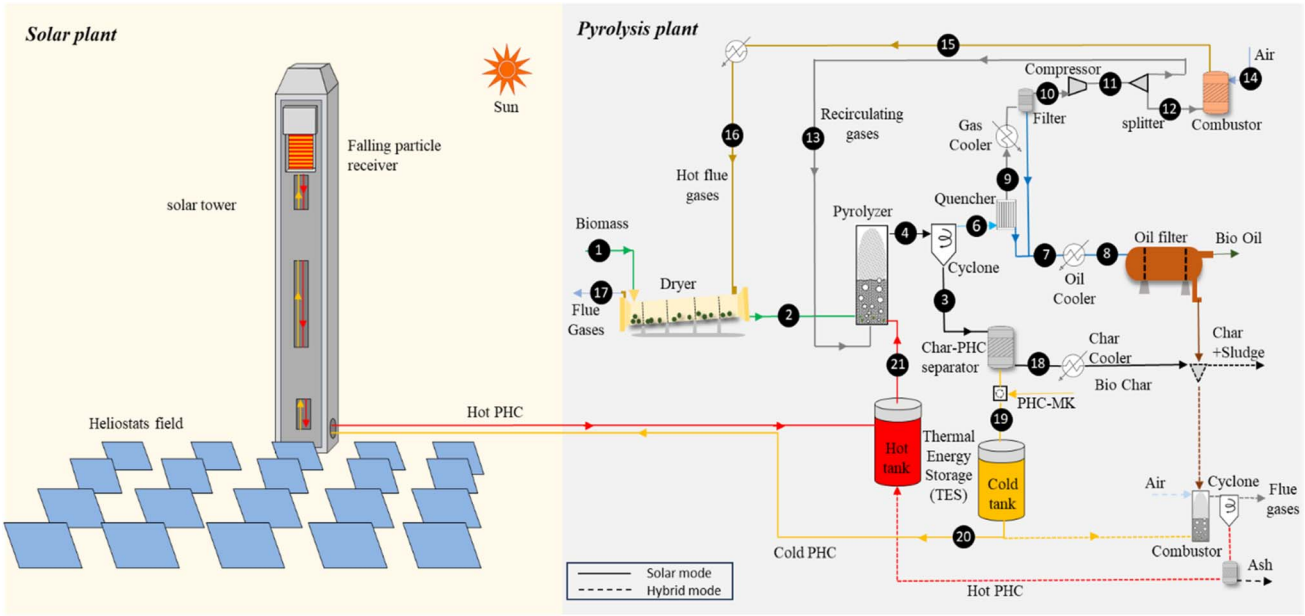

Fig. 3 Schematic diagram of the modelled CSP-based and hybrid pyrolysis plants. Dashed lines represent hybrid system operation when solar heat is not available.

irradiated by concentrated solar radiation to reach the temperature required by the pyrolysis process. After leaving the receiver, particles are sent to the pyrolizer and/or to the TES depending on the thermal power collected relative to the pyrolyzer need.

The plant is assumed to be located in Seville (Spain). DNI data are taken from SolarPILOT.[31] The thermal efficiency under any given condition is obtained using the in-house model described by Pasqualotto *et al.*[32] This model allows estimating the particle receiver thermal efficiency for a given geometry and given particle type and size. It accounts for the drag force effect on the particles, considers a 2D discretization of both solar flux on the receiver and particle properties inside the curtain, and considers the variable reflectivity of the wall behind the curtain. In this work, the sizing procedure is consistent with that used by Pasqualotto *et al.*,[32] while two types of PHCs are considered, namely CARBO ACCUCAST ID 50 (spherical sintered-bauxite particles) and sand, whose properties are shown in ESI Table 9.† ACCUCAST ID 50, used at Sandia Laboratories,[34] was identified as the best candidate for particle receivers due to its high solar absorptivity. However, sand is considered a lower-cost alternative[35] although featuring a considerably lower solar absorptivity, resulting in lower receiver thermal efficiency.

The design and simulation of the solar field are carried out using SolarPILOT.[31] Five solar field designs are considered by varying the solar multiple (SM). The SM characterizes the relative size of the CSP plant with respect to the pyrolysis plant, and it is defined as the ratio between the heat provided by the solar receiver in design conditions (*i.e.* 21st June, Solar noon) and the heat demand of the pyrolysis unit (1.73 MW_{th}):

$$SM = \frac{\dot{Q}_{PHC,rec}}{\dot{Q}_{PHC,pyro}}. \quad (7)$$

The tower height for different SM values is obtained by linear interpolation between 25 m for a 1.2 MW_{th} receiver, as reported by Coventry *et al.*,[36] and 55 m for a 20 MW_{th} receiver, as reported by Frantz *et al.*[37] All the other input parameters, presented in Table 3, are common for all the fields. The required incident power on the receiver for each solar field is determined by dividing the product of the pyrolizer power requirement and the theoretical value of the solar multiple (SM_T) with a guess value of thermal efficiency (assumed equal to 85% based on the thermal efficiency results obtained by Pasqualotto *et al.*[32]). However, it must be stressed that SM used in determining the required incident power on the receiver during the solar field sizing is, as aforementioned, only theoretical. This is because the actual value of SM depends on the actual design thermal efficiency of the receiver, which in turn depends, among others, on the type of PHC adopted. Therefore, the same solar field will have different actual SM values for Carbo ID 50 and sand. Aperture sizes for sizing each solar field are selected to meet a maximum flux of 2 MW m^{-2} (ref. 26) while keeping the average flux on the receiver equal to the conventional molten salts receiver (0.5 MW m^{-2} according to Blanco and Santigosa[39]). For the sake of simplicity, the receiver aspect ratio is assumed to be equal to one, as in the study by Pasqualotto *et al.*[32]

Table 3 Solar field design assumptions

Parameter	Value	References
Site	Seville	31
Latitude	37.4°	
Longitude	−5.9°	
Design DNI (W m^{-2})	900	
Design point	21st June, Solar noon	
Heliostat area (m^2)	16 (4 × 4 m)	38
Heliostat focusing type	At slant	38
Heliostat total reflected image error (mrad)	3.07	31
Heliostat reflectivity (—)	0.94	38
Design power to the HTM, SM = 1 (MW)	1.73	
First guess thermal efficiency (—)	0.85	

Fig. 4 represents solar fields generated using the previously described approach and their design optical efficiency (not considering the intercept efficiency, *i.e.* neglecting the "spillage" losses of reflected solar radiation that does not hit the receiver aperture due to manufacturing errors) for the cases with SM_T equal to 1, 5, and 9.

For each solar field and particle type, the optimal aperture size is selected to minimize in design conditions the trade-off between the spillage losses (complement of the intercept efficiency), and thermal losses, thus maximizing the design solar-to-thermal efficiency. Fig. 5 shows the values of solar-to-thermal efficiency for all considered sizes, SM_T, and particle types as a function of the receiver aperture size. Table 4 illustrates the design parameters of the best performing aperture sizes.

From the results presented in Table 4, it is possible to draw the following conclusions:

- Optical efficiency decreases with SM_T. This occurs because the cosine efficiency decreases as the average angle between the sun rays and the heliostat's surface normally increases more by adding new heliostats than it decreases by increasing the tower height.
- A considerable difference in the thermal efficiency (~11%) between Carbo ID 50 and sand is obtained due to the lower solar absorptivity of sand with respect to Carbo ID 50 (55% *versus* 90.6%).

Taking everything into account, solar-to-thermal efficiency decreases slightly with SM_T because an optical efficiency decrease has a higher impact than an increase in thermal efficiency. Additionally, Carbo ID 50 has ~8% higher value of solar-to-thermal efficiency compared to sand because of the differences in thermal efficiency. The actual SM values are obtained by dividing the design thermal power of the receiver by the thermal power required by the pyrolizer. The obtained thermal efficiency values for Carbo ID 50 are slightly higher than those reported in the literature for similar average heat flux on the receiver:[40] this is consistent with the lower receiver operating temperatures considered in this work (434–609 °C) compared to particle receivers in the literature, which are mainly designed for electricity generation purposes (operating at 550–750 °C).

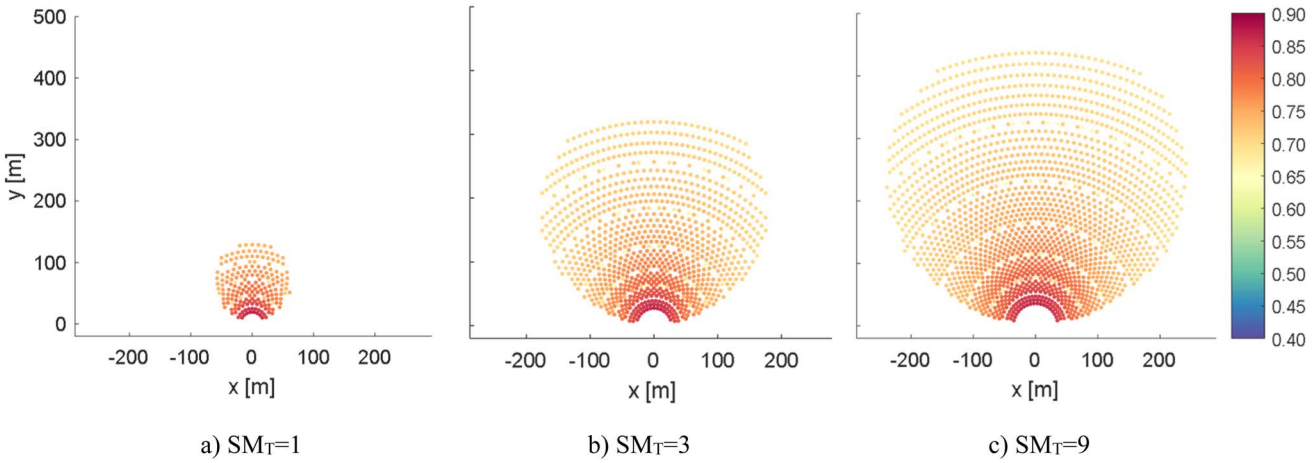

Fig. 4 Solar field layouts and heliostats optical efficiency for three values of SM_T.

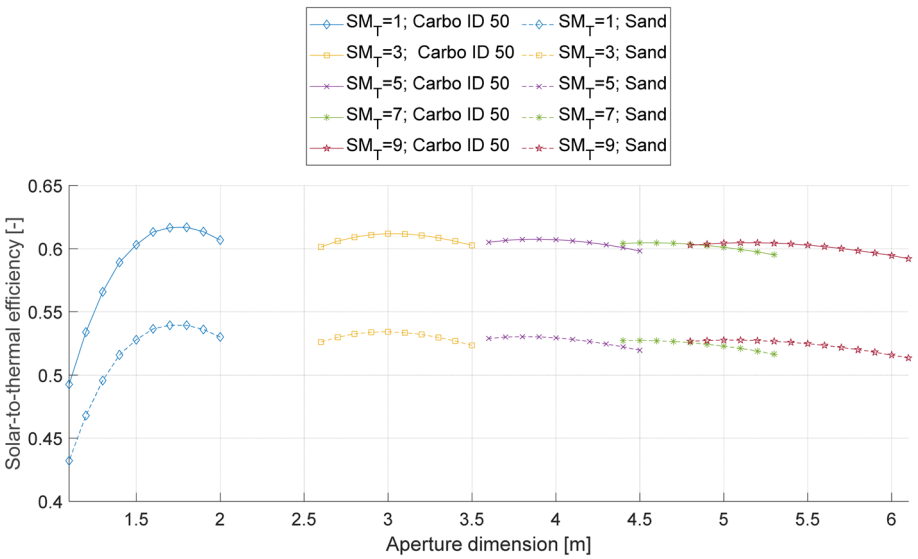

Fig. 5 Solar-to-thermal efficiency of bauxite and sand particles for different SM_T, as a function of the receiver aperture size.

Table 4 Design conditions of optimal receiver sizes

	$SM_T = 1$		$SM_T = 3$		$SM_T = 5$		$SM_T = 7$		$SM_T = 9$	
	Carbo ID 50	Sand	Carbo ID 50	Sand	Carbo ID 50	Sand	Carbo ID 50	Sand	Carbo ID 50	Sand
Tower height (m)	25.8		31.4		36.9		42.4		47.9	
Number of heliostats	191		591		996		1404		1801	
Cosine efficiency (%)	88.75		86.10		85.55		85.29		85.27	
Optical efficiency (%)	74.61	74.61	71.62	71.62	70.92	70.50	70.10	70.10	70.07	69.75
Thermal efficiency (%)	82.71	72.29	85.45	74.58	85.68	75.21	86.28	75.21	86.32	75.63
Aperture size (m)	1.8	1.8	3.0	3.0	3.9	3.8	4.5	4.5	5.1	5.0
Solar-to-thermal efficiency (%)	61.71	53.93	61.20	53.42	60.76	53.02	60.48	52.72	60.48	52.75
Receiver power (MW_{th})	1.702	1.488	5.262	4.601	8.858	7.743	12.460	10.906	16.072	14.062
Actual SM (—)	0.984	0.860	3.041	2.659	5.120	4.476	7.202	6.304	9.290	8.129

After defining the design of the solar field for each SM_T value, it is possible to compute the off-design performance of the receivers. The performance of each receiver is simulated by varying the DNI and thus the incident thermal power on the receiver from 0.2 to 1.15 of the nominal value while tuning the PHC flow rate to maintain a fixed temperature, which is equal to

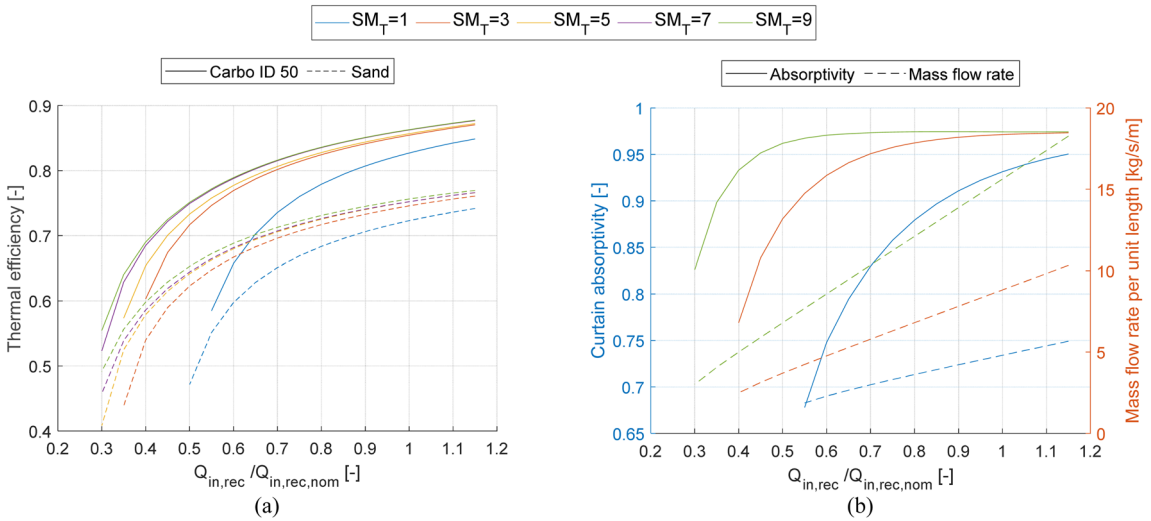

Fig. 6 (a) Thermal efficiency as a function of the relative thermal input for different solar multiple both for Carbo ID 50 and for sand and (b) curtain absorptivity and mass flow rate per unit length for three selected SM_T considering Carbo ID 50 as PHC.

the design value. The results of this analysis are shown in Fig. 6a as thermal efficiency curves *vs.* thermal input to the receiver relative to the nominal one ($Q_{in,rec}/Q_{in,rec,nom}$). The thermal efficiency of both Carbo ID 50 and sand decreases more quickly as the incident thermal power decreases for smaller SM_T. This is because the curtain absorptivity decreases more rapidly due to the lower mass flow rate per unit length for the smaller SM_T receivers, which is ultimately because the receiver aperture size grows less than proportionally with the SM_T (see Table 4). To better illustrate this, Fig. 6b shows the trends of the average absorptivity of the particle curtain and the mass flow rate per unit length of the receiver.

Solid PHC needs a lift to carry particles to the solar receiver from storage. The electrical power consumption for particle lift is calculated using eqn (8).[41] P_{lift} is the power required to lift PHC mass flow rate $\dot{m}_p$ in kg h^{-1} of solid particles to height H_{lift} in meters with an efficiency of η_{lift} that is considered as 0.8.[41] An additional 10% of overall electricity consumption is added to consider the consumption of light and other instruments related to the CSP plant.

$$P_{lift} = \frac{\dot{m}_p \times H_{lift} \times g}{\eta_{lift}}. \quad (8)$$

5. Hybrid pyrolysis

The CSP-based pyrolysis has drawbacks related to the daily and seasonal variability of solar energy, which does not allow for the continuous operation of the pyrolysis plant without major oversizing of the solar field and TES. Therefore, a *hybrid pyrolysis* case is introduced, where sludge and a fraction of the recovered char are burnt in the combustor to heat the PHC when solar energy is not available and the TES unit is empty.

The dashed lines in Fig. 3 illustrate the configuration when the plant is running in hybrid mode. This operating mode involves a reduction in the biochar output but allows for increasing the capacity factor of the pyrolysis plant, possibly improving the economic KPIs.

6. Economic analysis

The economic analysis is carried out for an N^{th}-of-a-kind plant, with assumptions and methodology consistent with NREL.[29,42] The method considers fixed and operational costs requiring the calculation of the yearly discounted cash flows and aims at identifying the Minimum Fuel (bio-oil) Selling Price (MFSP) to have an NPV equal to zero at the end of the plant lifetime. The iterative procedure is implemented in VBA Excel. The costs have been converted into euros at an exchange rate of 1.09 $ per €. The financial parameters are assumed to be consistent with the NREL reports. ESI Table 10† depicts a summary of the overall set of economic assumptions.[29]

The Net Present Value (NPV) is set to zero at the end of plant life with a fixed discount rate i, as shown in eqn (9):

$$NPV = -TCI + \sum_{t=-2}^{30} \frac{P_{by\text{-}prod,t} \times Q_{y\text{-}prod,t} + MFSP_t \times Q_t - T_t - C_{OP,VAR,t} - C_{OP,FIX,t} - L_{R,t}}{(1+i)^t} = 0, \quad (9)$$

where

- TCI represents the total capital investment for the pyrolysis and CSP plants (€),
- t is the year and includes a construction time of 3 years ($t = -2, -1, 0$),
- $MFSP_t$ represents the minimum selling price of the bio-oil (€ per t),
- Q_t represents the quantity of bio-oil produced per year (t per year),
- $P_{\text{by-prod},t}$ gives the unit selling price of the byproducts produced by the plant/year (€ per t),
- $Q_{\text{y-prod},t}$ represents the quantity of the byproducts produced by the plant/year (t per year),
- $C_{\text{OP,VAR},t}$ is the variable operational cost associated with the raw material and electricity per year (€ per year),
- $C_{\text{OP,FIX},t}$ is the fixed operational cost per year (€ per year),
- $L_{R,t}$ represents the interest paid on loan per year (€ per year),
- T_t represents the taxes paid for the year (€ per year).
- i is the discount rate (%).

According to data available in the literature,[43] the biochar price may vary significantly, ranging between 0.37 and 6.42 € per kg, with average wholesale and retail prices of 1.89 € per kg and 2.83 € per kg, respectively. For the calculation of MFSP, the average wholesale price of 1.89 € per kg is considered, subject to a sensitivity analysis.

6.1. Capital cost estimation

The Capex of the plant components is scaled with exponential law, as shown in eqn (10), where S_0 is the reference component size, S_X is the actual component size and n is the scaling factor, which is assumed to be 0.7.[29] The year 2019 is chosen as the reference year for the economic analysis, and eqn (11) allows for a discount of the component cost up to 2019 (C_{2019}) using the chemical engineering cost index CEPCI,[44] where $CEPCI_{2019}$ represents the cost index in 2019, which is 607.5 and $CEPCI_x$ shows the cost index in the reference year (see ESI Table 11†):

$$C_x = C_0 \times \left(\frac{S_X}{S_0}\right)^n, \tag{10}$$

$$C_{2019} = C_x \times \left(\frac{CEPCI_{2019}}{CEPCI_x}\right). \tag{11}$$

The total installed cost C_{inst} is estimated by multiplying the component cost by the installation factor (eqn (12)). The installation factor (ESI Table 11†) accounts for additional costs related to component installation, electrical network connections, control systems and civil work.

$$C_{inst} = f_{inst} \times C_{component} \tag{12}$$

The total direct plant cost is estimated by summing up the total installed cost with the cost of additional materials, costs of additional components, and site development cost, which are assumed to be 4.5%, 4% and 10% of component purchase cost, respectively.[29] The cost of land used to install the plant is also considered in the direct costs.

The overall cost of the pyrolizer, including the main reactor, cyclones, combustor, oil recovery system, compressors, and handling systems, is equal to 34.86 M€ for a capacity of 400 dry tons per day of treated biomass.[29,45] The cost of biomass pretreatment includes the dryer, entire handling area, handling system, storage system and biomass grinder, which is scaled from the literature[42] to our desired reference size and year. Similarly, the cost of utilities and auxiliary components, *e.g.* waste water treatment, cooling tower, products storage system, ventilation system, fire prevention system, and waste disposal system, is also considered (see ESI Table 11†). Apart from components costs, land cost was also considered assuming a pyrolysis plant footprint of 60 000 m^2 and an average land cost of 1.75 € per m^2.[46,47]

Indirect costs, accounting for 60% of the total direct costs, are used in this work. These costs include construction charges, legal expenses, engineering start-up and contingencies costs.

Fixed Capital Investment (FCI) of the CSP section is computed by summing up the heliostat field, receiver, tower, TES, particle and particle elevator costs, computed with correlations and reference values adapted from the literature (see ESI Tables 13 and 14†) according to eqn (13):

$$FCI = C_{hel,field} + C_{rec} + C_{tow} + C_{TES,hot} + C_{TES,cold} + C_{particles} + C_{elevator}. \tag{13}$$

6.2. Operational costs of pyrolysis plant

Operational costs for pyrolysis plants consider both fixed operational cost per year and variable operational cost. Variable operational cost includes biomass consumption, make-up cooling water, make-up sand, electricity and disposal of ash and waste water. The unit prices are obtained from the literature.[48] The biomass cost (17.05 € per t) is derived from the EIA database for biomass.[49] The estimation of the consumption of makeup and blow-down water for the cooling tower is based on the flow rate of cooling water, derived by Dutta *et al.*[48] The water consumption from this pyrolysis plant is scaled down according to this baseline study, which is approximately equal to 0.65 m^3 h^{-1}. The electrical power consumption for biomass pretreatment and grinding are assumed 50 kW h per t and 12 kW h per t, respectively.[50] An additional 10% of overall electricity consumption is considered for the consumption of light and other instruments. More details on the breakdown of variable operational costs are illustrated in ESI Table 15.†

The fixed operating costs include the wages of the employees and other expenses that are linked to the insurances, maintenance and taxes along with any other benefits and overheads. The annual costs related to the wages are estimated based on the data provided in ESI Table 16.†

6.3. Operational cost of CSP

According to Zaversky *et al.*,[51] the operational costs of a conventional CSP plant are equal to 1.5% per year of its TCI. However, due to the smaller size of the CSP plant and

Table 5 Mass flow rates, temperature, pressure, composition and carbon yield of input and output streams of the conventional pyrolysis plant shown in Fig. 2

					Composition (% wt)						
Streams name/no.	Stream description	Flow rate (kg h^{-1})	T (°C)	P (bar)	C	H	O	N	Ashes	PHC	% C yield
Input streams											
1	Biomass (wet)	2930	20	1.013	35.7	7.6	56.0	0.1	0.64	—	—
14	Combustion air	3829	32.2	1.013	0.01	0.2	24.8	75	—	—	—
25	Air to dryer	2094	32.2	1.013	0.01	0.2	24.8	75	0.00	—	—
PHC-MK	PHC make-up	3.2	32.2	—	—	—	—	—	—	100	—
Output streams											
12	Pyro-gas[a]	135	72.03	1.59	39.6	2.3	58.1	0.0	—	—	5
Bio-oil	Bio-oil	1732	54.4	1.24	41.6	7.8	50.6	0.0	—	—	69
17	Flue gases[b]	6969	71.7	1.013	3.9	1.4	30.9	63.8	—	—	26
Ash	Ash to disposal	22	608.4	—	—	—	—	—	85.6	14.4	—

[a] Molar composition of pyro-gas: 52% CO, 31% CO_2, 12% CH_4, 4% C_{2+}, 1% H_2. [b] Molar composition of flue gases: 63% N_2, 8.2% O_2, 9% CO_2, 19% H_2O, 0.8% Ar.

uncertainty regarding the reliability of the new technology, such as the falling particle receiver, in this work, operational costs are assumed to be equal to 2% per year of the TCI of the CSP plant. ESI Table 18† illustrates the operational cost breakdown of the solar power plant.

7. Results and discussions

7.1. Mass and energy balances under nominal operating conditions

In this section, the mass and energy balances of the baseline (conventional) and CSP-based pyrolysis plants at nominal conditions are presented. Further on, mass and energy balances of the CSP-based and hybrid plants are presented based on yearly balances for an economically optimized solar multiple.

7.1.1. Conventional pyrolysis plant. The flowrates, compositions and carbon yield of the input and output streams of the conventional pyrolysis plant are shown in Table 5. The carbon yield shows that the bio-oil contains 69% of the inlet carbon, in which 26% of the carbon is emitted to the atmosphere as CO_2 in combustion products and the remaining 5% is contained in the exported pyro-gas. ESI Table 19† illustrates the main properties of the plant streams (*e.g.* temperature, pressure, flow rate, and phase).

Table 6 Main thermodynamic results and energy balance of the conventional pyrolysis plant

Parameter	Value
Biomass input (kW_{LHV})	10 000
Bio-oil production (kW_{LHV})	7574
Pyro gas production (kW_{LHV})	362
Heat rejected to ambient (kW)	1986
Heat losses at combustor and pyrolyzer (kW)	200
Compressor electric power (kW)	118
Electric consumption for heat rejection (kW)	15
Electric consumption for biomass pretreatment (kW)	200
Other auxiliaries consumption (kW)	34
Energy conversion efficiency, $\eta_{pyro\ plant}$ (%)	73.9%
Carbon efficiency, ε_C (%)	74.1%
Emission to oil ratio, ETO ($kg_{CO_2}\ GJ_{oil}^{-1}$)	36.5
Net emission to oil ratio, ETO_{net} ($kg_{CO_2}\ GJ_{oil}^{-1}$)	0.0

Table 6 shows the energy balance and the main performance indicators of the conventional pyrolysis plant. Along with 10 MW_{LHV} of input biomass, 0.1 MW of electricity is consumed to run compressors and heat rejection auxiliaries for the pyrolysis process. The chemical energies contained in bio-oil and pyro-gas are 7.57 MW_{LHV} and 0.36 MW_{LHV}, respectively. Heat losses from the plant units (*e.g.* pyrolyzer, combustor, compressor and filters) are equal to 2.18 MW, accounting for almost 22% of total input biomass LHV. Heat dissipation losses also occur during quenching at the dryer outlet and char gas and oil cooling processes. The energy conversion efficiency of 73.9% demonstrates that even a conventional pyrolysis process can retain a substantial portion of the input biomass energy in the form of produced bio-oil and pyro-gas. A carbon efficiency of 74.1% indicates that most of the carbon in the biomass is retained in useful products rather than being emitted as CO_2. However, a significant portion is emitted into the environment due to the combustion of by-products. In general, the biomass conversion process is carbon neutral, so the net emission is still considered zero.

7.1.2. CSP-based pyrolysis. Compared to the conventional pyrolysis plant, two additional outlet streams appear: sludge and char. Consequently, a lower amount of carbon is lost as CO_2 to the atmosphere, corresponding to 9.3% of the carbon content of the feedstock (*vs.* 26% of the conventional pyrolysis case). This substantial reduction highlights the enhanced carbon sequestration capabilities of solar-based pyrolysis. The carbon content in bio-oil and pyro-gas streams remains the same as in conventional pyrolysis plant. The produced biochar contains 19.6% of the inlet carbon feedstock. This biochar can be used as a soil amendment, contributing to long-term carbon sequestration and improving soil quality. The properties of the input and output streams are shown in Table 7. Additional streams are reported in ESI Table 20.†

Table 7 Mass flow rates, temperature, pressure, composition and carbon yield of input and output streams in solar-based pyrolysis shown in Fig. 3

Streams name/no.	Stream details	Flow (kg h^{-1})	T (°C)	P (bar)	Composition (% mass) C	H	O	N	Ashes	PHC	% C yield
Input streams											
Biomass	Biomass (wet)	2930	20	1.013	35.7	7.6	56.0	0.1	0.64	—	—
14	Combustion air	3659	25	1.59	0.0	0.0	23.5	76.5	—	—	—
PHC-MK	PHC make-up	3	25	1.22	—	—	—	—	—	100	—
Output streams											
Bio-oil	Boi-oil	1732	54.4	1.24	41.6	7.8	50.6	0.0	—	—	69.0
Biochar	BioChar	246	25	1.22	83.1	1.7	6.6	1.4	7.1	—	19.6
Sludge	Sludge	59	54.4	1.24	38.3	7.2	46.6	—	2.4	5.4	2.2
17	Flue gases[a]	4555	71.7	1.013	2.1	1.7	34.7	61.5	—	—	9.3

[a] Molar composition of flue gases: 58.8% N_2, 12.8% O_2, 4.8% CO_2, 23% H_2O, 0.7% Ar.

Table 8 Main thermodynamic results and energy balance of the CSP-based pyrolysis plant

Parameter	Value
Biomass input (kW_{LHV})	10 000
Concentrated solar power (kW)	1730
Bio-oil production (kW_{LHV})	7574
Char production (kW_{LHV})	1998
Sludge production (kW_{LHV})	238
Heat rejected to ambient (kW)	1847
Heat losses at combustor and pyrolyzer (kW)	200
Compressor electric power (kW)	124
Electric consumption for heat rejection (kW)	15
Electric consumption for biomass pretreatment (kW)	200
Other auxiliaries consumption (kW)	34
Electric consumption for PHC lift (kW) [$SM_T = 1$]	5.1
Energy conversion efficiency, $\eta_{pyro\ plant}$ (%)	78.6%
Carbon efficiency, ε_C (%)	90.7%
Emission to oil ratio, ETO ($kg_{CO_2}\ GJ_{oil}^{-1}$)	13.06
Net emission to oil ratio, ETO_{net} ($kg_{CO_2}\ GJ_{oil}^{-1}$)	−27.5

Table 8 illustrates the energy balance and the main performance indicators of the CSP-based pyrolysis plant. In solar-based pyrolysis, the CSP block provides 1730 kW_{th} to the pyrolyzer by transferring thermal power through the PHC. Electrical power consumption, biomass, oil LHV and heat dissipation are similar to the conventional pyrolysis plant. Char and sludge chemical power are additional outputs that lead to an increase in energy efficiency ranging from 73.9% to 78.6%, indicating a more effective use of the input biomass energy. The additional energy input from concentrated solar power (CSP) helps to achieve this gain in efficiency. Carbon efficiency improves from 74.1% to 90.7%, meaning that a greater proportion of biomass carbon is retained in useful products (bio-oil and biochar). This higher carbon efficiency reflects the lower carbon losses and better utilization of feedstock biomass carbon.

The emission to oil ratio significantly decreases from 36.5 to 13.1 $kg_{CO_2}\ GJ_{oil}^{-1}$, demonstrating a reduction in the carbon footprint of the produced bio-oil. Moreover, the net negative emissions of −27.5 $kg_{CO_2}\ GJ_{oil}^{-1}$ indicate that the process can act as a carbon sink, removing more CO_2 from the atmosphere. In terms of energy content, the production of char and sludge contributes 1998 kW_{LHV} and 238 kW_{LHV}, respectively.

In the hybrid pyrolysis plant, the stream flows are the same as in the CSP-based case, provided hot PHC is available from the receiver or form the high-temperature PHC storage. When hot PHC is not available, sludge and almost 75% char are sent to the combustor to provide an alternative heat source for the PHC, as shown in Fig. 3.

7.2. Economic analysis

7.2.1. Conventional pyrolysis plant. The total estimated investment cost for the conventional pyrolysis plant is 20.25 M€, while total operating and maintenance costs are 2.99 M€ per year at 100% capacity factor of the pyrolysis plant (8760 h per year), as shown in Table 9. The resulting minimum fuel sale price of the bio-oil is 0.433 € per kg_{oil} or 27.53 € per GJ (LHV = 15.75 MJ kg^{-1}).

7.2.2. CSP-based pyrolysis plant. The CAPEX of the CSP-based plants depends on the size of the CSP plant (*i.e.* the SM_T) and the TES size. In this study, various sizes of the CSP plant and storage are analyzed, ranging from SM_T 1 to 9 and from 2 to 48 h of storage size, respectively. The capacity factor of the pyrolysis plant increases with TES size and SM_T and reaches the 70–90% range with SM_T of 5 and higher and TES capacity of 14–16 h (see ESI Fig. 1† for more details). The capacity factor (CF) is also linked to the energy usage efficiency of the CSP plant. Larger SM_T values at lower storage sizes waste more energy because they produce more than the storage can hold, and the excess energy is wasted (see ESI Fig. 2†). As shown in Fig. 7a, with an SM_T of 5 and higher, the MFSP decreases significantly up to 14–16 hours of storage and then continues decreasing but with a much lower slope. This is because ~16 h of storage guarantees enough stored energy to operate continuously all night for most of the summer days. Thus, a further increase in TES size improves the product yield in a limited number of days. For the CSP-based plant, 24 h is chosen as the TES size, and the corresponding solar multiple that minimizes the MFSP results is SM_T of 7. Lower SM_T involves high

Table 9 Costs, revenues, material quantities and MFSP of CSP and pyrolysis plant in conventional, CSP-based and hybrid cases

Components	Conventional M€	CSP based M€	Hybrid M€
Pyrolysis plant CAPEX (TCI)	**20.25**	**19.43**	**21.11**
Plant (pyrolizer and oil recovery system)	8.53	8.53	8.53
Solid char combustor	0.94	—	0.94
Gas combustor	—	0.48	0.48
Biomass pretreatment	1.24	1.24	1.24
Utilities and auxiliaries	0.48	0.48	0.48
Material stock up	0.17	0.16	0.17
Additional components	0.19	0.18	0.19
Site development	0.42	0.40	0.43
Land cost for pyrolysis plant	0.10	0.10	0.10
Indirect cost	7.23	6.94	7.54
Working capital	0.96	0.93	1.01
CSP plant CAPEX[a]	**—**	**6.51**	**4.82**
Heliostat field	—	3.32	2.35
Receiver	—	0.69	0.49
Tower	—	0.20	0.15
Thermal energy storage (TES)	—	0.72	0.68
PHC particle	—	0.04	0.04
PHC elevator cost	—	0.16	0.09
Land cost for CSP plant	—	0.3	0.2
Indirect cost & contingencies	—	1.07	0.79
Total CAPEX	**20.25**	**25.94**	**25.93**
Pyrolysis plant total O&M/year	2.99	2.86	3.02
Variable operational cost (biomass)/year	0.34	0.28	0.34
Variable operational cost (other materials & disposal)/year	0.23	0.19	0.23
Fixed operational cost/year	2.42	2.39	2.45
CSP plant O&M/year	—	0.13	0.1
Total O&M/year	**2.99**	**3.0**	**3.1**
Biochar revenues/year	0	3.36	3.31
Bio oil revenues/year[b]	6.58	4.29	4.46
Total revenues/year	6.58	7.65	**7.78**
Material flows (kt per year)	**Conventional**	**CSP based**	**Hybrid**
Biomass consumption (kt per year)	25.7	20.6	25.7
Bio-oil production (kt per year)	15.2	12.8	15.2
Sludge production (kt per year)	0	0.44	0.38
Pyro-gas (kt per year)	1.2	0	0
Char (kt per year)	0	1.8	1.8
CO_2 emissions (kt per year)	8.7	2.6	4.5
ETO ratio (kg_{CO_2} GJ_{oil}^{-1})	**36.5**	**13.1**	**19.0**
Net ETO ratio (kg_{CO_2} GJ_{oil}^{-1})	0	−27.5	−22.3
MFSP (€ per GJ)	27.53	21.79	18.68

[a] The values of CSP plant CAPEX are at the selected size of CSP plant based on MFSP. [b] This revenue is based on the MFSP of oil at the selected plant size.

costs due to the low capacity factor of the pyrolysis plant, which remains below 55% with SM_T 3, even with very large TES. The type of PHC has a small influence on the MFSP, except for low SM_T and relatively high TES size.

The total CAPEX of the CSP unit of the selected plant (SM_T 7, sand, 24 h TES) is 6.51 M€ (Table 9), which corresponds to about 25% of the total plant cost. The total operational and maintenance cost, including the electricity required to run the lift and other components, is 0.13 M€ per year (Table 9). The total CAPEX and O&M costs of the pyrolyzer for this case are slightly lower than for the conventional case because the combustor size is significantly smaller than the conventional one. For this case, the CAPEX and O&M costs of pyrolyzer are 19.43 M€ and 2.86 M€ per year, respectively (Table 9), while feedstock, consumable and utility costs (*e.g.* biomass, water, electricity, and disposal cost) depend on the capacity factor, which is around 82% at the selected size of CSP. The calculated MFSP is 0.34 € per kg_{oil} or 21.79 € per GJ.

7.2.3. Hybrid pyrolysis plant. Fig. 7b shows the dependency of the MFSP on the SM_T and TES size for the hybrid plant. The MFSP is much less sensitive to the TES size and solar multiple compared to the CSP-based plant, as a high capacity factor for the pyrolysis unit can be achieved independently of the sizing of the CSP unit. The selected case for the economic analysis has SMT 5, 22 h of storage and uses sand as PHC. The calculated MFSP for this case is 0.29 € per kg_{oil} or 18.68 € per GJ. This MFSP value is the lowest among all the above cases. This is because of the increased plant availability and the additional production of biochar, which also increases the profit margin. The annual revenues of the biochar in the CSP-based and hybrid pyrolysis plants are provided in Table 9. The total CAPEX for the selected CSP plant is 4.82 M€ (Table 9). Similarly, the total operational and maintenance cost, including the electricity required to run the lift and other components, is almost 0.1 M€ per year (Table 9). The CAPEX and O&M costs of the pyrolyzer for the hybrid case are slightly higher than those of the conventional and CSP-based cases, as it comprises two combustors (solid char and gas combustor). The CAPEX and O&M costs of the pyrolyzer of the hybrid case are 21.11 M€ and 3.02 M€ per year, respectively (Table 9).

Despite lower bio-oil production in CSP-based plants (12.8 kt per year *vs.* 15.2 kt per year for the conventional plant), the process is economically competitive thanks to the additional revenues from biochar production. The CSP-based and hybrid plants generate significant additional revenue from biochar (1.07 M€ per year and 1.2 M€ per year, respectively), thereby offsetting the higher capital and operational costs. This additional income contributes to the economic feasibility of the solar-based pyrolysis systems.

7.3. Operation profiles

In the CSP-based plant, the pyrolysis plant operates at full load during the summer days. Due to high insulation, the TES is never fully discharged and part of the solar radiation is lost when the TES system is fully charged. On winter days, the low solar radiation is such that the pyrolysis plant operates with a low capacity factor and a limited capacity of the TES system is exploited. Low radiation during cloudy or winter days and defocusing losses during summer due to overproduction remain challenges for high energy efficiency and better optimization of CSP systems. Although TES helps reduce losses and improve the stability of the process, prolonged seasonal variations still impose limitations on CSP-based pyrolysis operations, particularly during the winter and cloudy weeks.

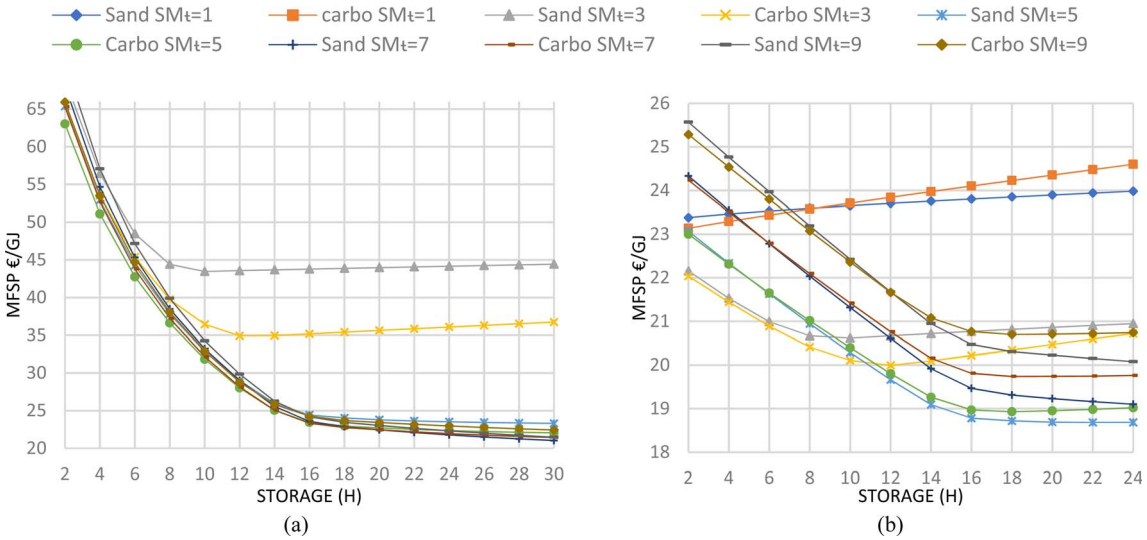

Fig. 7 MFSP of the CSP-based pyrolysis plant (a) and the hybrid pyrolysis plant (b) at various SM_T and storage sizes.

However, in the hybrid plant, the pyrolysis unit operates stably owing to the combustion of sludge and biochar in the low radiation hours. This alternative approach helps to achieve the maximum capacity factor of the pyrolysis process. However, on winter days, the CSP system barely contributes to the heat supply, which is mostly sustained by biochar combustion, which is why CO_2 emissions during winter are higher than those in summer. Fig. 8a shows the hourly variation in the CSP-based plant on 2 summer days (1–2 June), while Fig. 8b shows the production during winter days (19–20 Jan). Similarly, Fig. 9a and b show the same profiles for the hybrid plant. Q_PHC represents the energy transferred to PHC from the CSP plant at any specific hour of the day, while the Q_pyro indicates the energy that the pyrolyzer is consuming in its operations. Q_TES shows the energy stored in the TES unit, and Q_L indicates the lost solar energy in dissipation when the TES system is full. For the hybrid plant, Q_Comb shows the heat generated by the combustion of sludge and biochar.

7.4. Product yield and carbon balance

Fig. 10 shows the carbon balance for the three selected plants based on the yearly operation. The carbon balances of the conventional and CSP-based plants are the same as those shown in Section 7.1, as this is not affected by the operation profile. The carbon balance of the hybrid plant depends closely on the CSP plant sizing and its operating profile. For the selected sizing in the hybrid plant, 26% and 19% of sludge and char, respectively, are consumed from total annual production to meet the pyrolyzer energy demand, leading to a yearly carbon efficiency of 83% and specific emissions of 19.0 $kg_{CO_2}\ GJ_{oil}^{-1}$ (*vs.* 13.1 $kg_{CO_2}\ GJ_{oil}^{-1}$ of the CSP-based plant). As biogenic CO_2 emissions can be considered climate neutral, the CSP-based and hybrid processes remove an equivalent amount of CO_2 of 5.56 kt_{CO_2} per year and 5.34 kt_{CO_2} per year as biochar from the atmosphere, corresponding to net negative specific emissions of −27.5 and −22.3 $kg_{CO_2}\ GJ_{oil}^{-1}$, respectively (see Table 9).

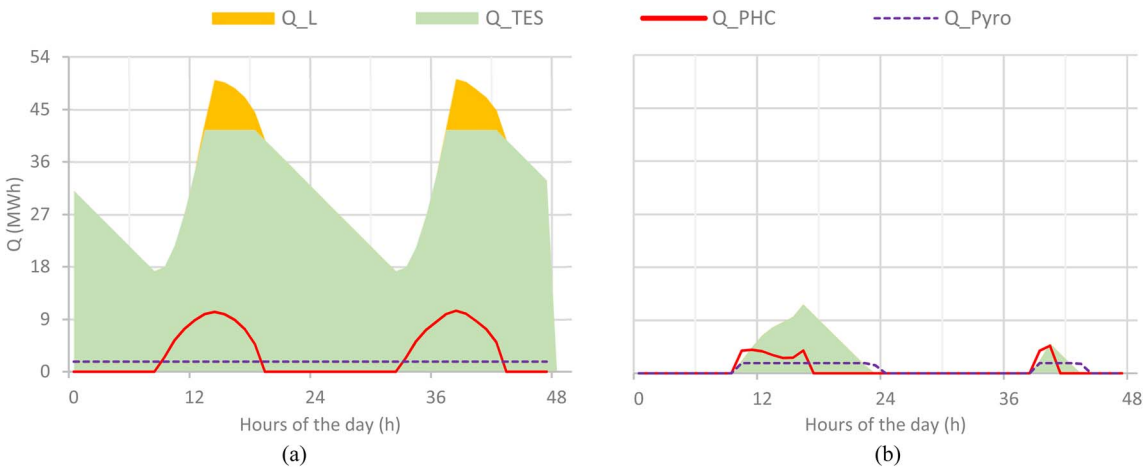

Fig. 8 Daily operation of the CSP-based pyrolysis plant with sand PHC, SM_T 7 and 24 h TES size. Charts refer to (a) summer days (1–2 June) and (b) partially cloudy winter days (19–20 Jan). Q_PHC: energy transferred from CSP to PHC; Q_TES: stored energy; Q_L: lost solar energy; Q_Pyro: energy used in the pyrolyzer.

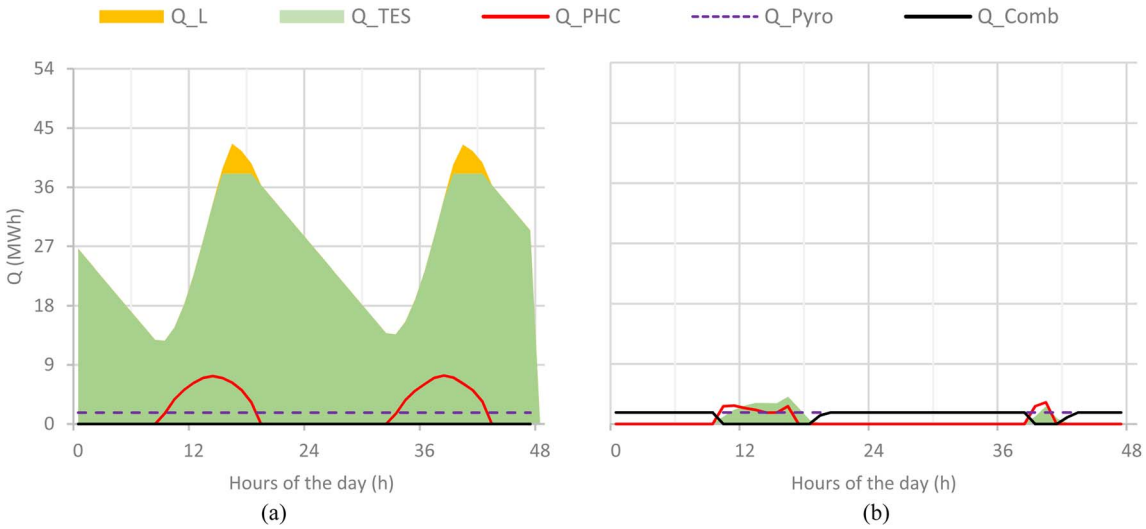

Fig. 9 Daily operation of the hybrid CSP pyrolysis plant with sand PHC, SMT 5 and 22 h TES size. Charts refer to (a) summer days (1–2 June) and (b) partially cloudy winter days (19–20 Jan). Q_PHC: energy transferred from CSP to PHC; Q_TES: stored energy; Q_L: lost solar energy; Q_Pyro: energy used in the pyrolyzer; Q_Comb: energy generated by sludge and char combustion.

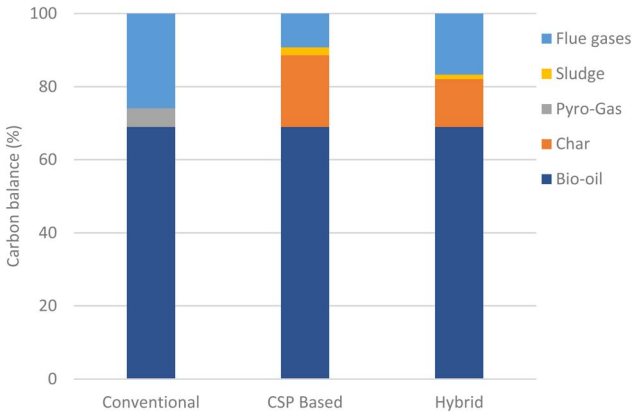

Fig. 10 Annual carbon balance of the assessed cases.

Fig. 11a shows the capacity factor of the pyrolysis plant and the monthly product yield. The plant capacity factor is limited to below 71% from November to February, while it peaks to above 95% in July and August. Bio-oil and biochar productivity as well as CO_2 emissions reflect the plant capacity factor trend.

Fig. 11b shows the monthly production and emission trends of the hybrid plant. As the hybrid plant runs stably throughout the year, the capacity factor of the pyrolysis unit is always 100%, and bio-oil yield depends only on the number of days in each month. In this plant, solar radiation affects biochar production and CO_2 emissions. In the winter months, when the plant relies more on biochar combustion, biochar yield is reduced and CO_2 emissions increase. The sizing of the solar field and the TES significantly affects the product yield and the carbon balance. ESI Fig. 3a and b† show the CO_2 emission trends with respect to SM_T and storage size of CSP-based and hybrid pyrolysis, respectively.

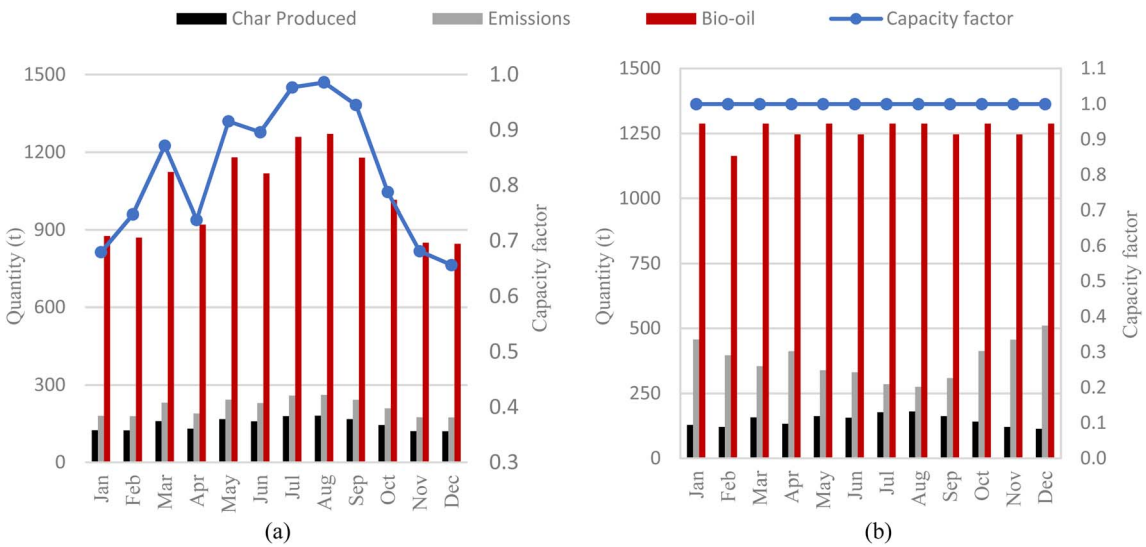

Fig. 11 Monthly distribution of products, emissions and availability in (a) CSP-based pyrolysis case and (b) hybrid pyrolysis at optimized scenarios.

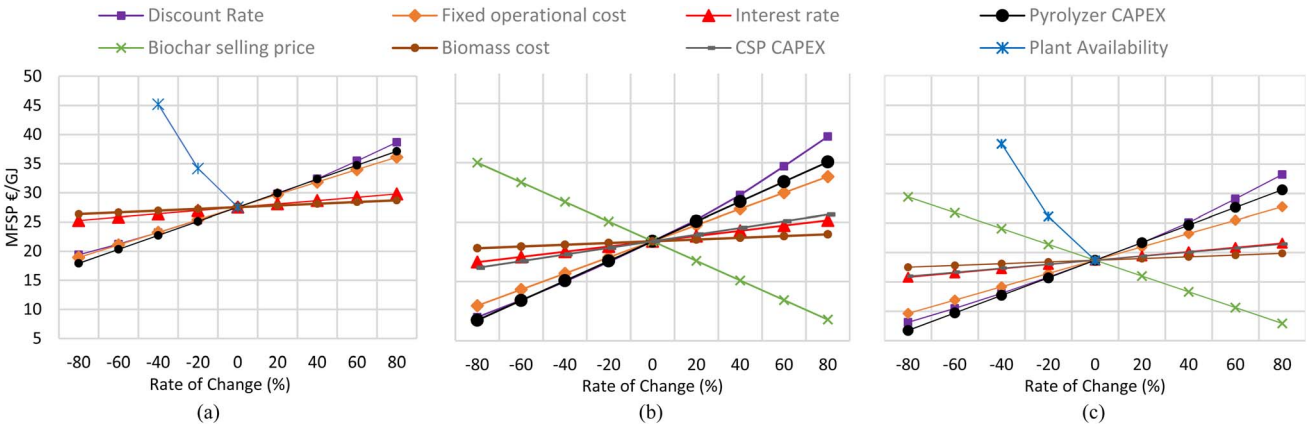

Fig. 12 Sensitivity analysis of MFSP under rate of change of different variables for (a) conventional pyrolysis plant, (b) CSP-based pyrolysis plant and (c) hybrid CSP pyrolysis plant.

7.5. Sensitivity analyses

To analyze the effect of multiple economic parameters on MFSP, a sensitivity analysis is also performed for the three considered plants, as shown in Fig. 12. For the conventional pyrolysis case, the plant availability has the most significant impact on the MFSP: a 40% reduction in operational hours means an almost 64% increase in MFSP. Similarly, the total fixed cost of pyrolyzer and discount rate have a notable impact on MFSP: a 40% increase in DR and plant cost can increase MFSP by almost 17%.

In the CSP-based plant, the availability varies based on the SM_T and storage size and its analysis is shown in Fig. 7a. The analysis in Fig. 12b refers to the selected optimized case. The DR and Pyrolyzer CAPEX have a significant impact, as in the conventional pyrolysis case. For example, a 60% decrease in DR, taxes and pyrolyzer Capex can decrease MFSP by almost 40% and *vice versa*. The fixed operational cost is the second most important factor because a 60% change in the rate can cause almost a 37% change in MFSP. The biochar selling price also significantly affects the MFSP. A variation between −80 and +80% (*i.e.* from 0.38 to 3.4 € per kg) involves a reduction in the MFSP from about 35 to 8.6 € per $GJ_{bio\text{-}oil}$. The other parameters, including the CSP plant cost, have a lesser impact on the MFSP (Fig. 12b).

Fig. 12c shows the same analysis for hybrid cases with similar trends. Decreasing availability by 40% increases the MFSP by almost 106%. Due to the lower production of biochar, its selling price affects the MFSP less than in the CSP-based plant: the variation between −80 and +80% leads to a reduction from 29.4 to 7.93 € per $GJ_{bio\text{-}oil}$.

The main additional source of revenues for CSP-based and hybrid cases is biochar. Fig. 13 shows that biochar selling prices of at least 1.24 and 0.64 € per kg (corresponding to carbon credits that are equal to 407 € per t_{CO_2} and 210 € per t_{CO_2}, respectively) make CSP-based and hybrid pyrolysis competitive with conventional pyrolysis.

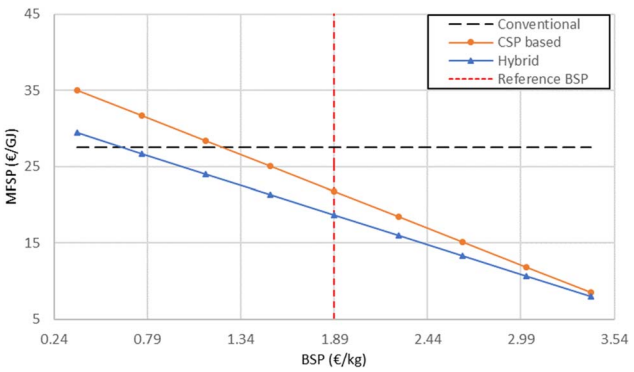

Fig. 13 MFSP variation with respect to biochar selling price for CSP-based and hybrid pyrolysis plants.

7.6. Significance, limits and future prospective

This study explored the potential of CSP-driven pyrolysis, demonstrating lower production costs and reduced CO_2 emissions compared to conventional pyrolysis relying on biochar combustion. This study showed that CSP-based and hybrid configurations can reduce carbon emissions by 70% and 48% and lower the production cost of bio-oil by 21% and 32%, respectively, compared to conventional pyrolysis. These results justify research and development efforts aimed at developing and understanding the technology from experimental and modelling perspectives.

This study relied on a simplified pyrolysis model with a constant product yield. Future research activity should focus on the development and implementation of detailed validated pyrolysis reactor models, including chemical kinetics, to evaluate the impact of the operational parameters (temperature, pressure, feedstock, residence time and heating rate) on the product yield and the solar section design. Additionally, PHC-char separation needs to be experimentally assessed and numerically modeled, as the separation efficiency affects the quality of biochar for end use as well as the heat transfer properties of the PHC in the solar receiver. Moreover, the performance of different PHCs through modelling and experimental activities needs to be assessed.

8. Conclusions

This study examined a 10 MW biomass pyrolysis plant in which the heat for the pyrolysis reactor, instead of being produced through by-product combustion, is provided by a CSP tower with a free-falling solid particle receiver. The pyrolysis plant is modeled in Aspen Plus, while the CSP solar field and solid particle receiver are modeled with Solar PILOT and specific in-house codes, respectively. Three types of process configurations have been investigated: a reference biomass pyrolysis process; a solar-based plant, where all the heat is supplied by the CSP system; and a hybrid solution, where most of the heat is supplied by the CSP system and by-product combustion as back-up. CSP and hybrid cases are studied with yearly simulations with hourly resolution, considering various solar multiples and storage sizes. Moreover, two types of PHC, sand and commercially available CARBO ACCUCAST ID 50, were analyzed. These analyses allowed us to obtain the annual performance, optical and thermal efficiencies of solar CSP, annual production and emissions from each scenario. The main conclusions of the study can be summarized as follows:

➢ Solar-based pyrolysis can achieve over 90% carbon efficiency, resulting from about 70% of the inlet biogenic carbon retained in the bio-oil and about 20% of the carbon in the biochar. Based on yearly simulations, the hybrid plant results in a carbon efficiency of 83%. The conventional pyrolysis process achieves 74% carbon efficiency. Owing to the carbon stored in biochar, the solar-based and hybrid plants achieve net negative emissions of −27.5. and −22.3 kg_{CO_2} GJ_{oil}^{-1}, respectively.

➢ For the hybrid plant, with an assumed biochar selling price of 1.89 € per kg, a minimum bio-oil selling price of 18.68 € per GJ_{LHV} was obtained, *vs.* 27.53 € per GJ_{LHV} of the reference pyrolysis process. For the CSP-based plant, the estimated MFSP is equal to 21.79 € per GJ_{LHV}. The cost of bio-oil produced in the CSP-based plant is higher than in the hybrid case despite the higher char yield due to the higher impact of Capex caused by the lower yearly capacity factor (82% *vs.* 100% of the hybrid case). Therefore, an economic-environmental trade-off exists between CSP-based and hybrid configurations, driven by minimum fuel selling price (*i.e.* fuel production cost) and overall process carbon efficiency.

➢ The sensitivity analysis showed that the variation of the discount rate, plant availability, biomass cost, biochar selling price and pyrolyzer CAPEX exhibits the highest impact on the MFSP. However, the type of particle heat carrier (sand or Carbo ID50 PHC) has a minor impact on the MFSP.

➢ The breakeven biochar selling prices for CSP-based and hybrid cases that can make them economically competitive with conventional pyrolysis are 1.24 € per kg and 0.64 € per kg, which correspond to carbon credit values of 407 € per t_{CO_2} and 210 € per t_{CO_2}, respectively.

Abbreviations

Capex	Capital expenditure
CSP	Concentrated solar power
DR	Discount rate
DSR	Dissipated solar radiation
ETO	Emission to oil ratio
FBR	Fluidized bed reactor
FCI	Fixed capital investment
HHV	Higher heating value
HTF	Heat transfer fluid
HTM	Heat transfer material
LHV	Lower heating value
MFSP	Minimum fuel sale price
NREL	National Renewable Energy Laboratories
PC	Product combustion
PHC	Particle heat carriers
SM_T	Theoretical solar multiple
TCI	Total capital investment
TDC	Total direct cost
TES	Thermal energy storage
TIC	Total installed cost
TPC	Total purchase cost
VBA	Visual basic analysis

Symbols

A_h	Total heliostats area [m^2]
C_{inst}	Installation cost [€]
$C_{component}$	Component cost [€]
C_o	Cost of reference component size [€]
C_x	Cost of selected component size [€]
$C_{hel,field}$	Cost of heliostat & field [€]
C_{rec}	Cost of receiver [€]
C_{tow}	Cost of tower [€]
$C_{TES,hot}$	Cost of hot thermal energy storage [€]
$C_{TES,cold}$	Cost of cold thermal energy storage [€]
$C_{particles}$	Cost of PHC particles [€]
$C_{elevator}$	Cost of PHC elevator [€]
$C_{OP,VAR,t}$	Variable operational cost per year [€ per year]
$C_{OP,FIX,t}$	Fixed operational cost per year [€ per year]
DNI	Direct normal irradiance [W m^{-2}]
E	CO_2 emissions [kg s^{-1}]
ε_C	Carbon efficiency [—]
f_{inst}	Installation factor [—]
g	Gravitational acceleration [m s^{-2}]
H_{lift}	Height of PHC lift [m]
i	Discount rate [%]
LHV_{biom}	LHV of biomass [MJ kg^{-1}]
$LHV_{prod,i}$	LHV of the i^{th} product [MJ kg^{-1}]
$L_{R,t}$	Loan with the inclusion of interest paid per year [€ per year]
$\dot{m}_{biom}$	Mass flow rate of biomass [kg s^{-1}]
$\dot{m}_{prod,i}$	Mass flow rate of the i^{th} product [kg s^{-1}]
$\eta_{pyro\ plant}$	Pyrolysis plant energy conversion efficiency -
m_p	PHC mass flow rate [kg s^{-1}]
n	Scaling factor [—]
$\eta_{el,ref}$	Electric efficiency [—]
η_{sol-th}	Solar-to-thermal efficiency [—]
η_{opt}	Optical efficiency [—]
$\eta_{th,rec}$	Thermal efficiency [—]

$\eta_{th,use}$	Thermal energy usage efficiency [—]
η_{lift}	Lift efficiency [—]
Oil	Oil production [kg s^{-1}]
P_{Aux}	Electric power used by auxiliaries [W]
$P_{by\text{-}prod,t}$	Selling price of by-products per year [€ per year]
P_{lift}	Electric power used by PHC lift [W]
$\dot{Q}_{def}$	Total solar power loss by defocusing [W]
$\dot{Q}_{PHC,pyro}$	Thermal power provided to pyrolyzer *via* PHC [W]
$\dot{Q}_{PHC,rec}$	Thermal power delivered to PHC [W]
$\dot{Q}_{rec}$	Solar power incident on the receiver [W]
Q_t	Quantity of bio-oil produced per year [t per year]
$Q_{y\text{-}prod,t}$	Quantity of the byproducts produced per year [t per year]
S_0	Reference component size [t per day]
S_X	Selected component size [t per day]
T_t	Taxes paid per year [€ per year]
$y_{C,biom}$	Carbon content of biomass [%]
$y_{C,prod,i}$	Carbon content in the i^{th} product [%]

Data availability

The data supporting this article have been included as part of the ESI.†

Conflicts of interest

There are no conflicts to declare.

Acknowledgements

This study is funded by the European Union under Pysolo project (Grant Agreement n. 101118270). Views and opinions expressed are however those of the author(s) only and do not necessarily reflect those of the European Union or CINEA. Neither the European Union nor the granting authority can be held responsible for them.

References

1 R. Adib, *Renewables 2023 Global Status Report Collection, Renewables in Energy Supply*, 2023.
2 A. M. Elgarahy, A. Hammad, D. M. El-Sherif, M. Abouzid, M. S. Gaballah and K. Z. Elwakeel, Thermochemical conversion strategies of biomass to biofuels, techno-economic and bibliometric analysis: A conceptual review Ahmed, *J. Environ. Chem. Eng.*, 2021, **9**, 2213–3437, DOI: **10.1016/j.jece.2021.106503**.
3 L. L. Berkel, P. Debiagi, H. Nicolai, M. A. Amjed, A. Stagni, C. Hasse and T. Faravelli, Development of a multiphase chemical reactor network method as a tool for simulating biomass gasification in fluidized beds, *Fuel*, 2024, **357**, 129731, DOI: **10.1016/j.fuel.2023.129731**.
4 S. F. Javaid, *et al.*, Production of Biochar by Slow and Solar-Biomass Pyrolysis: Focus on the Output Configuration Assessment, Adaptability, and Barriers to Market Penetration, *Arabian J. Sci. Eng.*, 2024, 1–20, DOI: **10.1007/S13369-023-08549-3**.
5 M. Muhyuddin, P. Mustarelli and C. Santoro, Recent Advances in Waste Plastic Transformation into Valuable Platinum-Group Metal-Free Electrocatalysts for Oxygen Reduction Reaction, *ChemSusChem*, 2021, **14**(18), 3785–3800, DOI: **10.1002/cssc.202101252**.
6 M. A. Amjed, *et al.*, Surface decoration and characterization of solar driven biochar for the removal of toxic aromatic pollutant, *J. Chem. Technol. Biotechnol.*, 2021, **96**(8), 2310–2324, DOI: **10.1002/jctb.6759**.
7 V. Chintala, Production, upgradation and utilization of solar assisted pyrolysis fuels from biomass – A technical review, *Renewable Sustainable Energy Rev.*, 2018, **90**, 120–130, DOI: **10.1016/j.rser.2018.03.066**.
8 T. Hosseini and L. Zhang, Process modeling and techno-economic analysis of a solar thermal aided low-rank coal drying-pyrolysis process, *Fuel Process. Technol.*, 2021, **220**, 106896, DOI: **10.1016/j.fuproc.2021.106896**.
9 G. J. Nathan, *et al.*, Solar thermal hybrids for combustion power plant: A growing opportunity, *Prog. Energy Combust. Sci.*, 2018, **64**, 4–28, DOI: **10.1016/j.pecs.2017.08.002**.
10 M. A. Amjed, *et al.*, Recent Updates on the Solar-Assisted Biochar Production and Potential Usage for Water Treatment, *Fresenius Environ. Bull.*, 2020, **29**(07A), 5616–5632.
11 K. Zeng, D. Gauthier, D. P. Minh, E. Weiss-Hortala, A. Nzihou and G. Flamant, Characterization of solar fuels obtained from beech wood solar pyrolysis, *Fuel*, 2017, **188**, 285–293, DOI: **10.1016/j.fuel.2016.10.036**.
12 M. U. H. Joardder, P. K. Halder, A. Rahim and N. Paul, Solar Assisted Fast Pyrolysis: A Novel Approach of Renewable Energy Production, *J. Eng.*, 2014, **1**, 252848, DOI: **10.1155/2014/252848**.
13 M. A. Rahman, A. M. Parvej and M. A. Aziz, Concentrating technologies with reactor integration and effect of process variables on solar assisted pyrolysis: A critical review, *Therm. Sci. Eng. Prog.*, 2021, **25**, 100957, DOI: **10.1016/j.tsep.2021.100957**.
14 S. Guillén-Lambea and M. Carvalho, A critical review of the greenhouse gas emissions associated with parabolic trough concentrating solar power plants, *J. Cleaner Prod.*, 2021, **289**, 125774, DOI: **10.1016/j.jclepro.2020.125774**.
15 X. Li, Y. Shen, X. Kan, T. K. Hardiman, Y. Dai and C. H. Wang, Thermodynamic assessment of a solar/autothermal hybrid gasification CCHP system with an indirectly radiative reactor, *Energy*, 2018, **142**, 201–214, DOI: **10.1016/j.energy.2017.09.149**.
16 H. Wu, D. Gauthier, Y. Yu, X. Gao and G. Flamant, Solar-Thermal Pyrolysis of Mallee Wood at High Temperatures, *Energy Fuels*, 2018, **32**(4), 4350–4356, DOI: **10.1021/acs.energyfuels.7b03091**.
17 S. Morales, R. Miranda, D. Bustos, T. Cazares and H. Tran, Solar biomass pyrolysis for the production of bio-fuels and chemical commodities, *J. Anal. Appl. Pyrolysis*, 2014, **109**, 65–78, DOI: **10.1016/j.jaap.2014.07.012**.
18 R. Aparecida da Silveira Rossi, J. M. Barbosa, M. Antonio de Souza Barrozo and L. G. Martins Vieira, Solar assisted catalytic thermochemical processes: pyrolysis and hydropyrolysis of Chlamydomonas reinhardtii microalgae,

Renewable Energy, 2021, **170**, 669–682, DOI: 10.1016/j.renene.2021.02.034.

19 R. Li, *et al.*, Product distribution from solar pyrolysis of agricultural and forestry biomass residues, *Renewable Energy*, 2016, **89**, 27–35, DOI: 10.1016/j.renene.2015.11.071.

20 K. Zeng, D. P. Minh, D. Gauthier, E. Weiss-Hortala, A. Nzihou and G. Flamant, The effect of temperature and heating rate on char properties obtained from solar pyrolysis of beech wood, *Bioresour. Technol.*, 2015, **182**, 114–119, DOI: 10.1016/j.biortech.2015.01.112.

21 V. Chintala, S. Kumar, J. K. Pandey, A. K. Sharma and S. Kumar, Solar thermal pyrolysis of non-edible seeds to biofuels and their feasibility assessment, *Energy Convers. Manage.*, 2017, **153**, 482–492, DOI: 10.1016/j.enconman.2017.10.029.

22 J. Zeaiter, M. N. Ahmad, D. Rooney, B. Samneh and E. Shammas, Design of an automated solar concentrator for the pyrolysis of scrap rubber, *Energy Convers. Manage.*, 2015, **101**, 118–125, DOI: 10.1016/j.enconman.2015.05.019.

23 C. Ghenai, K. Alamara and A. Inayat, Solar Assisted Pyrolysis of Plastic Waste: Pyrolysis oil Characterization and Grid-Tied Solar PV Power System Design, *Energy Procedia*, 2019, **159**, 123–129, DOI: 10.1016/j.egypro.2018.12.029.

24 A. Peinado Gonzalo, A. Pliego Marugán and F. P. García Márquez, A review of the application performances of concentrated solar power systems, *Appl. Energy*, 2019, **255**, 113893, DOI: 10.1016/j.apenergy.2019.113893.

25 M. Mehos, *et al.*, *Concentrating Solar Power Gen3 Demonstration Roadmap*, 2017, DOI: 10.2172/1338899.

26 J. Christian and C. Ho, Design requirements, challenges, and solutions for high-temperature falling particle receivers, *AIP Conf. Proc.*, 2016, **1734**(1), DOI: 10.1063/1.4949060.

27 J. L. Jie Ling, E. S. Go, Y.-K. Park and S. H. Lee, Recent advances of hybrid solar - Biomass thermo-chemical conversion systems, *Chemosphere*, 2021, **290**, 133245, DOI: 10.1016/j.chemosphere.2021.133245.

28 *Pysolo Project*, https://pysolo.eu/, accessed Oct. 20, 2023.

29 S. Jones, *et al.*, *Process Design and Economics for the Conversion of Lignocellulosic Biomass to Hydrocarbon Fuels: Fast Pyrolysis and Hydrotreating Bio-Oil Pathway*, 2013.

30 *Aspentech*, https://www.aspentech.com/en/products/engineering/aspen-plus, accessed Feb. 22, 2022.

31 M. J. Wagner and T. Wendelin, SolarPILOT: A power tower solar field layout and characterization tool, *Sol. Energy*, 2018, **171**, 185–196, DOI: 10.1016/j.solener.2018.06.063.

32 O. Pasqualotto, F. Sobic, G. Gentile, M. Binotti, A. Giostri and G. Manzolini, A falling particle receiver thermal model for system-level analysis of solar tower plants, *Sol. Energy*, 2024, **268**, 112117, DOI: 10.1016/J.SOLENER.2023.112117.

33 T. Anton, J. D. McNatt and L. Krahn, *Thermal properties of wood and wood panel products for use in buildings (No. DOE/OR/21697-1)*, Forest Products Lab, 1988, Forest Service, Madison, WI (USA), DOI: 10.2172/6059532.

34 C. K. Ho, J. Christian, J. Yellowhair, S. Jeter, M. Golob, C. Nguyen, K. Repole, S. Abdel-Khalik, N. Siegel, H. Al-Ansary, A. El-Leathy and B. Gobereit, Highlights of the high-temperature falling particle receiver project: 2012 - 2016, *AIP Conf. Proc.*, 2017, **1850**, DOI: 10.1063/1.4984370.

35 M. Mehos, *et al.*, *Concentrating Solar Power Gen3 Demonstration Roadmap*, 2017, DOI: 10.2172/1338899.

36 J. Coventry, C. Andraka, J. Pye, M. Blanco and J. Fisher, A review of sodium receiver technologies for central receiver solar power plants, *Sol. Energy*, 2015, **122**, 749–762, DOI: 10.1016/j.solener.2015.09.023.

37 C. Frantz, R. Buck and L. Amsbeck, Design and Cost Study of Improved Scaled-Up Centrifugal Particle Receiver Based on Simulation, *J. Energy Resour. Technol.*, 2022, **144**(9), 092107, DOI: 10.1115/1.4053784.

38 A. Giostri, M. Binotti, C. Sterpos and G. Lozza, Small scale solar tower coupled with micro gas turbine, *Renewable Energy*, 2020, **147**, 570–583, DOI: 10.1016/j.renene.2019.09.013.

39 M. J. Blanco and L. R. Santigosa, *Advances in Concentrating Solar Thermal Research and Technology*, 2016.

40 L. F. González-Portillo, K. Albrecht and C. K. Ho, Techno-Economic Optimization of CSP Plants with Free-Falling Particle Receivers, *Entropy*, 2021, **23**(1), 76, DOI: 10.3390/E23010076.

41 L. F. González-Portillo, K. Albrecht and C. K. Ho, Techno-economic optimization of CSP plants with free-falling particle receivers, *Entropy*, 2021, **23**(1), 76, DOI: 10.3390/e23010076.

42 S. Phillips, A. Aden, J. Jechura, D. Dayton and T. Eggeman, *Thermochemical Ethanol via Direct Gasification and Mixed Alcohol Synthesis of Lignocellulosic Biomass, Technical Report NREL/TP-510-41168*, NREL, Natl. Renew. Energy Lab., 2007, p. 125, http://www.nrel.gov/docs/fy07osti/41168.pdf.

43 *International Biochar Initiative*, https://biochar-international.org/state-of-the-biochar-industry-2014/, accessed Feb. 22, 2023.

44 *Chemical Engineering Annual Index*, https://www.chemengonline.com/, accessed Feb. 19, 2023.

45 N. Nikolopoulos, *et al.*, Report on comparison among current industrial scale lignite drying technologies (A critical review of current technologies), *Fuel*, 2015, **155**, 86–114, DOI: 10.1016/j.fuel.2015.03.065.

46 C. Nickerson, M. Morehart, T. Kuethe, J. Beckman and J. Ifft, *Trends in U.S. Farmland Values and Ownership*, 2012.

47 USDA and NASS, *Land Values 2017 Summary*, 2017.

48 A. Dutta, *et al.*, *Process Design and Economics for the Conversion of Lignocellulosic Biomass to Hydrocarbon Fuels. Thermochemical Research Pathways with In Situ and Ex Situ Upgrading of Fast Pyrolysis Vapors*, NREL, 2015, p. 275, http://www.osti.gov/servlets/purl/1215007/.

49 *Feedstocks and Average Cost Per Ton for the Manufacture of Densified Biomass Products*, US Energy information administration. https://www.eia.gov/biofuels/biomass/#table_data, accessed Feb. 19, 2023.

50 M. M. Wright, D. E. Daugaard, J. A. Satrio and R. C. Brown, Techno-economic analysis of biomass fast pyrolysis to transportation fuels, *Fuel*, 2010, **89**(SUPPL. 1), S2–S10, DOI: **10.1016/j.fuel.2010.07.029**.

51 F. Zaversky, *et al.*, Techno-Economic Optimization and Benchmarking of a Solar-Only Powered Combined Cycle with High-Temperature TES Upstream the Gas Turbine, in *Green Energy and Environment*, 2020.

